THE WHITE DWARF OPPORTUNITY

THE WHITE DWARF OPPORTUNITY: CONSTRAINING STELLAR WINDS FROM THE GALAXY'S MOST COMMON STARS USING A WHITE DWARF COMPANION

By RAVEN WESTLAKE, BSc

A Thesis Submitted to the School of Graduate Studies in Partial Fulfillment of the Requirements for the Degree Master of Science

McMaster University

MASTER OF SCIENCE (2025)

Hamilton, Ontario, Canada (Physics and Astronomy)

TITLE:	The White Dwarf Opportunity: Constraining Stellar Winds from the Galaxy's most Common Stars Using a White Dwarf Companion
AUTHOR:	Raven Westlake BSc (Mathematical Physics), Trent University, Peterborough, Canada
SUPERVISOR:	Dr. Ryan Cloutier and Dr. Alison Sills
NUMBER OF PAGES:	xiii, 109

Abstract

The winds of M dwarf stars are poorly constrained and poorly understood. Literature values of M dwarf wind mass-loss rates span several orders of magnitude and suffer from poor number statistics, with fewer than 30 systems having well-constrained values. Stellar winds are especially important to how young planetary systems evolve, with consequences for expected exoplanet atmosphere loss, atmospheric chemistry, surface habitability, and more. While several methodologies exist for constraining stellar winds, only four have produced detections of wind mass-loss rates for M dwarf stars. One of these methodologies involves constraining the M dwarf mass-loss rate using atmospheric metal pollution of a close companion white dwarf star. In this work, I calculate wind mass-loss rates for two M dwarf stars using this methodology. Additionally, I expand the range of systems to which this methodology can be applied. Previous studies have noted that M dwarfs in close binary systems with white dwarfs are often magnetically active. This magnetic activity produces emission lines for magnetically sensitive elements, such as calcium. Calcium is also the metal pollutant that produces the deepest optical light absorption signals in white dwarfs. In this work, I develop methodology for recovering calcium absorption equivalent widths from white dwarf stars in unresolved binaries with magnetically active M dwarfs. I apply this methodology to 56 systems, recovering 19 white dwarf calcium equivalent widths

which remain in absorption within their 1σ uncertainty. While it is left to a future work to calculate wind rates for these systems, this methodology does significantly expand the number of close white dwarf-M dwarf binary systems for which M dwarf wind rates can be recovered.

Acknowledgements

I would like to thank my supervisors, Dr. Ryan Cloutier and Dr. Alison Sills, without whom this thesis would not have been possible. I have grown a lot as a scientist thanks to the past two years of their guidance and I am very grateful to have had this opportunity. I would also like to thank the members of my committee, Dr. Laura Parker and Dr. Doug Welch for the time and energy they invested into the thesis defense process. The thorough and informative feedback they provided greatly improved the flow and clarity of this thesis. I would also like to thank Dr. Simon Blouin who used his polluted white dwarf models to calculate the calcium abundances for two stars, making it possible for me to calculate wind rates for those two systems.

I greatly appreciate the support of my friends, family, and partner over the past two years. It truly does take a village, and I wound not be where I am today without you. I would also like to thank the McMaster physics and astronomy community, who have filled these past two years with wonderful memories. I wouldn't trade these experiences for anything, you are the reason McMaster is such a wonderful place.

Lastly, I acknowledge that McMaster University is located on the traditional territories of the Mississauga and Haudenosaunee nations, and within the lands protected by the "Dish with One Spoon" wampum agreement. I would like to give thanks for being able to work on this land.

Table of Contents

List of Figures

List of Tables

Notation and Abbreviations

Notation

q	The mass ratio between the White Dwarf and M Dwarf: $\frac{M_{MD}}{M_{WD}}$
M_{WD}	The mass of the White Dwarf
M_{MD}	The mass of the M Dwarf
R_{MD}	The radius of the M Dwarf
$F_{cont.}$	The flux of the continuum
F_{total}	The total flux
$F_{MD_{H\alpha}}$	The flux of the M dwarf Hα emission line
$F_{MD_{cont.}}$	The flux of the M dwarf continuum
$M_{\odot}$,$R_{\odot}$	Solar mass and radius
R_{Roche}	Roche radius
p_{orb}	orbital period

ρ	density (of the M dwarf wind material)
a	Separation (of the binary pair)
G	gravitational constant (value)
v_{rel}	relative velocity of the White dwarf compared to the M dwarf wind material
v_{orb}	orbital velocity
v_{wind}	velocity of the M dwarf wind material
Ca/H	calcium abundance (N(Ca)/N(H))
$\mathbf{(Ca/H)_\odot}$	solar calcium abundance (2.1875×10^{-6}) (Debes, 2006)
Θ	diffusion timescale of calcium in the white dwarf atmosphere
q_{conv}	White dwarf convective zone mass fraction
$\dot{M}_\odot$	Solar mass loss rate (2×10^{-14} approximate solar mass loss rate from Wood 2021, units of $M_\odot$/yr)

Abbreviations

BHL	Bondi-Hoyle-Lyttleton
Ca II K	Calcium II K
CV	Cataclysmic Variable
DA	Hydrogen Atmosphere White Dwarf

DAZ	Metal Polluted Hydrogen Atmosphere White Dwarf
DB	Helium Atmosphere White Dwarf
DZ	Metal Polluted White Dwarf
EDR	Early Data Release
EW	Equivalent Width
FWHM	Full-Width-Half-Maximum
HZ	Habitable Zone
ISM	Interstellar Medium
K-S	Kolmogorov-Smirnov
MESA	Modules for Experiments in Stellar Astrophysics
NAN	Not A Number
MCMC	Markov Chain Monte Carlo
PCEB	Post-Common-Envelope Binary
SDSS	Sloan Digital Sky Survey
WD	White Dwarf
WD+MD	White Dwarf-M Dwarf Binary
WDMS	White Dwarf-Main Sequence
XUV	X-ray and extreme Ultra Violet

Declaration of Academic Achievement

I declare that the contents of this thesis are my own original work, except as clearly indicated in the text.

Dr. Simon Blouin contributed to this work by fitting his polluted white dwarf models to two spectra to calculate the white dwarf calcium abundances of SDSS J015225.38-005808.5 and SDSS J184412.58+412029.4.

This thesis made use of data from the Sloan Digital Sky Survey white Dwarf-Main Sequence Binary Catalogue (Rebassa-Mansergas et al., 2012), supplemented with data from Morgan et al. (2012) and "A Modern Mean Dwarf Stellar Color and Effective Temperature Sequence" version 2022.04.16 (Pecaut & Mamajek, 2013) as described in section 2.2. Data was also used from the Sloan Digital Sky Survey Data Release 7 Spectroscopic M Dwarf Catalogue (West et al., 2011) as described in section 2.1. This thesis made use of the e-folding timescales and convective zone mass fractions of Bauer & Bildsten (2019) as described in section 2.2.

This work was partially funded by an Ontario Graduate Fellowship awarded by the Government of Ontario.

Chapter 1

Introduction

The most common stars in our Galaxy are the smallest of the main sequence stars, called M dwarfs. These stars are of particular interest in the search for extrasolar life due to their long lifetimes, high occurrence of closely orbiting rocky planets (Dressing & Charbonneau, 2015), and because planets around M dwarfs produce larger signals in exoplanet detection methods (such as the transit method and radial velocity method) than similar planets around Sun-like stars. For example, due to the larger planet/star radius ratio, planets transiting in front of an M dwarf are the best candidates for detailed atmospheric analysis via atmospheric transmission spectroscopy, observed by instruments such as the James Webb Space Telescope (Kopparapu et al., 2017). However, there are a few properties of M dwarf behaviour and evolution that can have significant impacts on the atmospheric escape, atmospheric chemistry, and habitability prospects of their planets, some of which are poorly understood. Some of the poorly understood properties are the evolution of the rotation period of M dwarfs, M dwarf magnetic activity (linked to rotation), and M dwarf stellar winds. Stellar winds govern angular momentum evolution and consequently magnetic evolution in

stars (Vidotto et al., 2014), so understanding how M dwarf stellar winds behave at the population level is crucial to improving our understanding of M dwarf evolution.

The population level distribution of M dwarf stellar wind mass-loss rates is not well understood and remains an important outstanding question. Current wind rate constraints are poor due to the difficulty of measuring the wind rates which are low density and have low photon counts, resulting in low number statistics (Kislyakova et al., 2024). I have found only 50 literature values for M dwarf wind mass-loss rates, excluding upper limits. These are sourced from four different methodologies and only cover only 29 unique systems, and are discussed further in section 1.1. For the methodology used in this thesis, only 10 systems have published M dwarf wind mass-loss rates. Debes (2006) (hereafter D06) and Walters et al. (2023) (hereafter W23) are the two works that report M dwarf wind mass-loss rates using this methodology. They have four overlapping systems and W23 provides two wind rates per system using different accretion models, for a total of 22 M dwarf wind mass-loss rates spanning nine orders of magnitude, which are discussed in section 1.3.

In this work, I aim to improve the population-level understanding of M dwarf stellar winds. I leverage a method of constraining M dwarf wind mass-loss rates in which photospheric pollution of a companion white dwarf (WD) star can be used to constrain the M dwarf mass-loss rate. Since pollutants settle rapidly out of the atmosphere of WDs, the risk of WD photospheric pollution from other sources is negligible. This method was introduced in D06, where M dwarf wind mass-loss rates were obtained for three close (< 1 AU) M dwarf - white dwarf binaries and three wide (> 1 AU) M dwarf - white dwarf binaries. Specifically, binary pairs containing a WD with a hydrogen dominated atmosphere and pollution absorption features of

elements heavier than helium (i.e. "metals") were used. This type of WD is called 'DAZ', where 'DA' is the spectral type of a WD with a hydrogen atmosphere and 'DZ' is the spectral type of a WD with metal lines in its spectrum. Key WD spectral types are summarized in table 1.4.

I refine the methodology of D06 for constraining M dwarf wind mass-loss rate via photospheric metal pollution of a close WD companion to work with unresolved systems, including those with M dwarf emission lines. I am able to recover WD absorption equivalent widths (EW) for 19 such systems at the 1σ level. While not calculated in this thesis, these EWs can be used in conjunction with polluted WD models to recover metal abundances, from which WD accretion rate and M dwarf wind mass-loss rate could be calculated. Additionally, I recover wind rates for two systems which displayed visible WD absorption. Once wind mass-loss rates are estimated for the 19 systems with WD absorption EWs, the collection of literature M dwarf wind mass-loss rates will be $\sim 40\%$ larger. The methodology improvements implemented in this work greatly increase the number of M dwarfs for which wind mass-loss rates can be recovered, and will contribute towards a better population level understanding of the distribution of M dwarf wind mass-loss rates.

1.1 Overview of M Dwarf Stars and Their Winds

M dwarf stars are the most common stars in the Milky Way Galaxy, comprising about 70% of the population (Henry et al., 2006; Winters et al., 2015) and ∼40% of the mass (Chabrier, 2003). M dwarf stars have masses as low as 0.08 $M_\odot$, the hydrogen burning limit, and as high as 0.6 $M_\odot$ (Chabrier et al., 1996; Baraffe & Chabrier, 1996). These stars frequently host habitable zone (HZ) exoplanets, where expected planet

surface temperatures are suitable for liquid water, but the true habitability of these planets remain uncertain (Zahnle & Catling, 2017). Due to their low mass, M dwarf stars have very long lifetimes, hundreds of times the current age of the Universe for a 0.1 $M_{\odot}$ star (Laughlin et al., 1997) and as low as $\sim$ 50 Gyr for the most massive M dwarfs (Tarter et al., 2007). Young M dwarfs emit elevated levels of X-ray and extreme ultraviolet (XUV) radiation due to their rapid rotation (Johnstone et al., 2021), which causes inflation of the atmospheres of their exoplanets (Owen & Wu, 2017).

Additionally, due to their low temperatures, M dwarf stars have the closest-in HZs of main-sequence stars, with orbital periods spanning $\sim$10-100 days for M0V - M6V stars (Newton et al., 2016). This close proximity to the stellar surface makes HZ planets around M dwarf stars more susceptible to atmosphere loss compared to HZ planets around FGK stars. M dwarf exoplanet atmospheres are subject to hydrodynamic escape (thermally driven bulk outflows of material) and non-thermal escape, such as that driven by stellar winds. Photoevaporation is the process by which gas is heated and ionized by high energy radiation, increasing the velocity of the gas particles away from the energy source. By heating the gas in exoplanetary atmospheres, stellar irradiation can cause photoevaporation to occur, resulting in exoplanet atmosphere loss. This is a form of hydrodynamic escape. Interactions between material in the atmosphere of an exoplanet and a stellar wind can also contribute to exoplanet atmosphere loss, a form of non-thermal escape. These processes can act independently or together, though the atmospheric escape can be amplified when both processes act together, with a heated and inflated exoplanet atmosphere being more susceptible to non-thermal escape processes, such as stellar wind stripping (Chin et al., 2024).

This is especially important during the elevated XUV radiation phase when the star is young, which inflates the exoplanet atmospheres (Lammer et al., 2007; Luger & Barnes, 2015). While the total amount of XUV radiation from an M dwarf is less than that from a higher mass Sunlike star, the closer in HZ of M dwarfs makes it such that the XUV radiation a HZ planet is exposed to over its lifetime is larger for an M dwarf HZ planet than a HZ planet around a Sunlike star (Johnstone et al., 2021).

Stellar winds are magnetically driven outflows of material launched from the outer layers of a star in a fast flowing stream (Johnstone et al., 2015). Stellar winds are composed of massive particles (protons, alpha particles, etc.), are highly ionized, and contain comparatively few photons (Wood et al., 2021). Telescope observations require photons, but the low wind densities of cool main sequence stars have not yet yielded detections via direct methods such as X-ray emission due to charge exchange with interstellar medium (ISM) neutrals or radio free-free emission. Currently, direct detection of stellar winds is not possible for cool main sequence stars other than the Sun. For all other FGKM stars, indirect diagnostics of stellar winds are used to provide measurements (Wood et al., 2021; Kislyakova et al., 2024). Indirect diagnostics of stellar winds rely on absorption or emission features caused by the interaction of the wind with a secondary component such as the ISM. These diagnostics are discussed in section 1.1.1.

Some works, such as Modi et al. (2023), find that stellar wind has a negligible effect on M dwarf exoplanet atmosphere loss ($< 5\%$ of H/He envelope lost in 5 Gyr), except for closely orbiting (< 0.2 AU) small exoplanets. Other works, such as Zendejas et al. (2010), find that there are some planet mass/atmosphere mass combinations that would allow HZ planets around early type M dwarfs to retain their

atmospheres for at least 1 Gyr, but that HZ planets around late type M dwarfs (later than M5V for their model) are less likely to retain their atmospheres due to their longer activity lifetimes. Since few measurements exist for M dwarf mass-loss rates, it is currently unclear if M dwarf winds fully strip their planets atmospheres often, or only occasionally. The missing piece in determining whether M dwarf HZ exoplanets are a promising place to look for extrasolar life is how windy M dwarfs are at the population level.

1.1.1 Measuring M Dwarf Stellar Winds

Current observational constraints on M dwarf stellar wind rates suffer from a strong bias towards nearby stars due to the relative faintness of M dwarfs to other main sequence stars (Bourrier et al., 2016; Debes, 2006; Kislyakova et al., 2024; Walters et al., 2023). Some indirect detection methods have strict constraints on distance and location of the star, such as requiring a partially ionized interstellar medium (Wood et al., 2021). There is also a potential bias towards M dwarfs with inherently higher wind mass-loss rates, as many indirect measurement techniques rely on the wind mass-loss rate to be high enough to produce secondary effects such as exoplanet atmosphere loss (Bourrier et al., 2016), or only work for active stars (Jardine & Collier Cameron, 2019) for which wind mass-loss rates tend to be higher (Wood et al., 2021). These biases make it challenging to determine what the wind mass-loss rates of M dwarfs are at the population level, especially in conjunction with the low total number of reported M dwarf wind mass-loss rates. Since stellar winds are magnetically driven, the magnetic effects of the M dwarf can be important to resultant M dwarf wind (W23). M dwarfs remain magnetically active for billions of years, so it is good to

understand the wind conditions of magnetically active M dwarfs.

Magnetic activity in the M dwarf refers to strong magnetic fields which heat the upper atmosphere and produce excess chromospheric and coronal emission. M dwarf stars can have particularly strong magnetic fields, on the order of kG, which produce excess coronal and chromospheric emission by heating their upper atmospheres (Morgan et al., 2012). In addition, M dwarf stars remain magnetically active for a very long time compared to earlier type stars. Activity lasts for an average of ∼1-2 Gyr for early spectral types (M0-M3) and 4-8 Gyr for late spectral types (M4-M7) (West et al., 2008). M dwarf stars span the transition from fully convective stars, below ∼0.35 $M_\odot$, and partially convective stars, above ∼0.35 $M_\odot$ (Chabrier & Baraffe, 1997). This transition region occurs between spectral types M3 and M4, and is the same as the division between "early" and "late" M dwarfs. Across all M dwarf spectral types, activity decreases as a function of age (Morgan et al., 2012). Stellar rotation appears to play an important role in a star's magnetic activity. The Skumanich age-rotation-activity relation (Skumanich, 1972), which was derived using mostly G dwarfs, shows that stars tend to spin down as they age due to angular momentum loss driven by magnetized stellar winds, and decrease in activity as a result. Isolated stars tend to have their rotational evolution tied to the lifetime of their circumstellar disk, with slower rotators resulting from longer-lived disks (Barnes & Sofia, 1996; Bouvier et al., 1997; Sills et al., 2000; Tinker et al., 2002). Despite different mechanisms for magnetic field generation in early and late M dwarf stars due to differences in their internal structure, the magnetic activity is expected to be correlated to the star's rotation, with more activity for faster rotators (Rebassa-Mansergas et al., 2013).

M dwarfs remain rapidly rotating ($<$ 10 days period) for 1-3 Gyr, but then display

a rapid spin-down with older M dwarfs rotating slowly (> 70 days period) (Pass et al., 2022, 2024). Very few M dwarfs are observed in the intermediate rotation period range ($10 - 70$ days), suggesting that there is significant and rapid angular-momentum loss. The cause of this rapid spin-down is not currently understood (Pass et al., 2024). Additionally, low mass M dwarfs ($\sim 0.08 - 0.25$ $M_\odot$) remain magnetically active for longer than higher mass M dwarfs (West et al., 2015). M dwarfs are known to display global magnetic fields, though the strength and axisymmetry of the large-scale field vary significantly as seen in figure 3 of Donati et al. (2023) and figure 11 of Wood et al. (2021). Magnetic channeling of winds allows for mass loss along magnetic field lines. While the total mass loss is low due to the low density of the winds, significant angular momentum may still be removed (Jardine & Collier Cameron, 2019).

Here I summarize the different methods of detecting M dwarf wind mass-loss rates:

Astrospheric Lyα Absorption

Stellar winds push away ISM material, forming a "bubble" around their host star. This ISM interaction region is called an astrosphere for stars with "weaker" stellar wind compared to O/B stars, and called a stellar-wind bubble for O/B stars (Wood et al., 2003). At the edge of the astrosphere, there is a buildup of ISM material, and a charge exchange occurs between protons in the wind and neutrals in the ISM, producing 'hot' hydrogen atoms which cause excess absorption in the wings of the stellar Lyman α line (Wood et al., 2005). Due to absorption from the ISM and the outermost region of Earth's envelope, the center part of the Lyman α line is not observable from near-Earth orbit. Therefore, the production of high-velocity neutral hydrogen atoms via the charge exchange between stellar wind protons and ISM

neutrals is essential to detectable Lyman α (Lyα) absorption in the wings (Kislyakova et al., 2024). These hydrogen atoms form what is called a hydrogen wall at the edge of the astrosphere. Stronger stellar winds form larger astrospheres, as they are more efficient at pushing away ISM material. A larger astrosphere results in a thicker hydrogen wall with a higher column density, leading to more Lyα absorption (Wood et al., 2021).

Wood et al. (2021) used this indirect wind diagnostic to measure wind rates for six M dwarf stars and upper limits for five. Combined with a previously constrained M dwarf wind rate from Wood et al. (2005), an astrosphere detection later reported in Vannier et al. (2025), and upper limits for a system previously constrained in Wood et al. (2001) there were a total of 14 M dwarf mass loss constraints (eight measurements and six upper limits). For 12 of these, the wind rates were found to be comparable to or weaker than the Sun's wind rate of $\sim 2 \times 10^{-14} M_{\odot}$ yr^{-1}. Wood et al. (2021) focused on early M dwarfs, which they expected to have stronger, more detectable winds due to having larger surface areas. When normalized by surface area, ten of the M dwarf wind mass-loss rates are comparable to or less than the Sun's surface area normalized wind mass-loss rate. The eight M dwarf systems with wind mass-loss rates determined using the astrospheric Lyα method are shown in table 1.1. Comparison between the wind rates found through various methods are shown in table A.1.

Table 1.1: M dwarf wind mass-loss rates for the eight systems where the wind rates were determined using the astrospheric Lyα method. For reference, the Sun's wind mass-loss rate is $\sim 2 \times 10^{-14}$ $M_\odot$ yr^{-1}
References: (1) Wood et al. (2005) (2) Vannier et al. (2025) (3) Wood et al. (2021)

Astrospheric Lyα Absorption Wind Rates			
Star Name	Spectral Type	Wind Mass-Loss Rate ($M_\odot$ / yr)	Ref.
EV Lac	M3.5	2×10^{-14}	1
GJ 173	M1	1.5×10^{-14}	2 & 3
GJ 338AB	M0 + M0	1×10^{-14}	3
YZ CMi	M4	6×10^{-13}	3
GJ 205	M1.5	6×10^{-15}	3
GJ 860AB	M3 + M4	3×10^{-15}	3
GJ 15AB	M2 + M3.5	2×10^{-13}	3
GJ 887	M2	1×10^{-14}	3

Slingshot Prominences

One method of indirectly measuring stellar wind mass-loss rates is by using 'slingshot' prominences. These transient features are visible as absorption in the hydrogen Balmer lines, and strong resonance lines such as Ca II H & K (Jardine & Collier Cameron, 2019). Although transient features may be visible in all these lines, the Hα line is most often used.

Cool star winds have a low density of outflowing plasma, which is a key barrier to their detection. Conveniently, active cool stars can display regions of higher-density outflowing plasma within their coronae, stellar 'slingshot' prominences. The winds of rapidly-rotating low-mass stars can be constrained using these 'slingshot' prominences. The closed magnetic loop structures of these active cool stars trap hot wind material near the co-rotation radius, where it gathers and cools. The material builds up until its mass can no longer be supported by the stellar magnetic field. Once the maximum mass is exceeded, the prominence ceases to be confined by the

stellar magnetic field and, depending on whether the prominence mass was originally supported above or below the star's co-rotation radius, it will either fall back towards the stellar surface, or be centrifugally ejected (Jardine & Collier Cameron, 2019).

These stars typically have very hot coronae, magnetically heated to temperatures of $10^6 - 10^7$ K, and many of them repeatedly form and eject slingshot prominences. The key for using slingshot prominences to estimate stellar mass-loss rates is that the upflows that feed a prominence supply mass to the prominence and the stellar wind at the same rate. Repeated observations of prominence masses and recurrence times can thus be used to estimate the mass-loss rate of the wind material. This method only works for rapidly rotating stars, and observations are biased towards ultra-fast rotators (Jardine & Collier Cameron, 2019). The fastest rotators among M dwarf stars tend to be the most active, and also have the highest wind mass-loss rates, so the applicability of wind measurements using slingshot prominences to M dwarf stars in general is highly limited. The ten M dwarfs with wind mass-loss rates determined using the slingshot prominence method are shown in table 1.2 (note that V374 Peg is observed in two different works). It should be noted that Waugh et al. (2021) identify a bias in determining an M dwarf wind mass-loss rate from slingshot prominence material. If a significant proportion of the prominence material is not visible, the prominence mass and by extension the wind mass-loss rate will be underestimated. They expect that this will be most significant for stars with large co-rotation radii.

Table 1.2: M dwarf wind mass-loss rates for the ten systems where the wind rates were determined using the slingshot prominence method.
References: (1) Jardine & Collier Cameron (2019) (2) Waugh et al. (2021)

Slingshot Prominence Wind Rates			
Star Name	Mass ($M_\odot$)	Wind Mass-Loss Rate ($M_\odot$ / yr)	Ref.
HK Aqr	0.4	1×10^{-12}	1
V374 Peg	0.3	4×10^{-12}	1
V374 Peg	0.3	2.4×10^{-11}	2
EQ Peg B	0.25	5.2×10^{-12}	2
GJ1156	0.14	1.1×10^{-14}, 8.4×10^{-15}, 1.2×10^{-14}	2
AD Leo	0.42	2.2×10^{-14}, 2.8×10^{-14}	2
EQ Peg A	0.39	1.4×10^{-12}	2
GJ1111	0.10	5.4×10^{-16}, 1.1×10^{-14}	2
GJ1245b	0.12	8.5×10^{-17}, 1.6×10^{-15}, 6.2×10^{-16}	2
GJ9520	0.55	3.6×10^{-14}	2
GJ494	0.59	1.7×10^{-15}, 2.8×10^{-14}	2

Absorption from Evaporating Exoplanetary Atmospheres

Interactions between close-in planets with their host star's stellar wind can be used to constrain the stellar wind properties (Vidotto & Bourrier, 2017). This method relies on simultaneous modeling of the stellar radiation pressure and winds interacting with the upper planetary atmosphere, matching the modeled transmission spectrum to observations of the star seen through the transiting planet's evaporating atmosphere (Vidotto & Bourrier, 2017). Bourrier et al. (2016) discuss observations of the exoplanet GJ 436 b, a roughly Neptune mass planet located 0.0287 AU (Butler et al., 2004; Gillon et al., 2007) from its M dwarf host star. They state that while the dynamics of the escaping gas are heavily influenced by radiation pressure of the host star, variations in the absorption signal–namely depth and duration–at different phases of the transits cannot be explained by radiation pressure alone.

Using numerical simulations, Bourrier et al. (2016) model the combined effects of

stellar radiation pressure and stellar wind on GJ 426 b's escaping upper atmosphere. While the goal of Bourrier et al. (2016) was to examine the coupled effects of stellar wind and stellar radiation pressure on the planet's exosphere, the planet's simulated atmosphere particles are subject to other physical effects such as stellar photoionization. They use 3D numerical models with their EVaporating Exoplanets (EVE) code to constrain local wind properties, which are then used by Vidotto & Bourrier (2017) to calculate the mass-loss rate of the host star. Vidotto & Bourrier (2017) find the wind rate to be $0.02 - 0.13$ times the Sun's wind mass-loss rate, consistent with the lowest non-upper-limit value from the astrospheric Lyα method of 0.15 times the Sun's wind mass-loss rate in Wood et al. (2021). The two M dwarf systems with wind mass-loss rates determined using the explanetary atmosphere evaporation method are shown in table 1.3.

Table 1.3: M dwarf wind mass-loss rates for the two systems where the wind rates were determined using the exoplanet atmosphere evaporation method. References: (1) Bourrier et al. (2016) (2) Vidotto & Bourrier (2017) (3) Alvarado-Gómez et al. (2022)

Exoplanetary Atmosphere Evaporation Wind Rates			
Star Name	Spectral Type	Wind Mass-Loss Rate ($M_\odot$ /yr)	Ref.
GJ 436	M2.5	0.45-2.5 $\times 10^{-15}$	1, 2
AU Mic	M1	$\sim$ 1-2 $\times 10^{-13}$	3

Radio Emission

Winds of giant stars have been directly detected via free-free emission at radio frequencies whose intensity scales with the temperature and density of the wind. For low-mass main sequence stars ($\lesssim 0.6$ M$_\odot$), only upper limits on wind mass-loss rates

have been obtained using radio emission, and these upper limits are tens to thousands of times the Sun's mass-loss rate. The low densities of cool MS stellar winds make them very difficult to measure through radio emission, and this difficulty is compounded by other emission effects at radio frequencies that are not related to the stellar wind properties, namely chromospheric thermal emission and coronal synchrotron emission (Bloot et al., 2025).

X-Ray Emission

Another method of constraining stellar winds of cool main-sequence stars is by detecting soft X-ray emission due to charge exchange between ions in the stellar wind and cold neutrals in the ISM. Where the astrosphere method relies on protons in the stellar wind colliding with neutral atoms or molecules in the astrosphere to create excess absorption in the wings of the Lyman α line, this X-ray emission method relies on ions instead of protons in the ionized wind, which capture electrons from the neutrals. An electron captured into an excited state then produces an XUV photon as it decays to the lowest available orbit. Soft X-rays from such interactions can be observed out to tens of parsecs from other stellar systems (Kislyakova et al., 2024).

While this method was successfully used on three K dwarfs in Kislyakova et al. (2024), it has only provided upper limits on stellar wind mass-loss rates for M dwarf systems thus far.

1.2 Overview of White Dwarf Stars

White dwarf stars are the remains of low to intermediate mass stars of initial masses up to ~ 9 $M_\odot$ (Kepler et al., 2007). The mass of a WD depends primarily on the

mass of its progenitor, with higher mass progenitors resulting in higher mass WDs. However, the lowest mass WDs come from binary evolution. The universe is not yet old enough for the smallest stars to leave the main sequence (Laughlin et al., 1997). Low mass (< 0.45 $M_\odot$) WDs form due to mass transfer in binary systems, and these tend to be helium core WDs (Sarna et al., 2001; Benvenuto & De Vito, 2005). Progenitors with masses between $\sim 1 - 7$ $M_\odot$ form WDs with masses between 0.45 $M_\odot$ and 1.05 $M_\odot$, which are usually carbon/oxygen core WDs, the most common core composition for WDs (Hansen, 2004). The distribution of carbon-oxygen core WDs peaks at ~ 0.6 $M_\odot$ (Hansen, 2004). For progenitors with masses between $\sim 7 - 9$ $M_\odot$, oxygen/neon core WDs are formed, with masses between ~ 1 $M_\odot$ and ~ 1.3 $M_\odot$ (Werner et al., 2005).

There exist many WD spectral types, which are based on the properties of the WD atmosphere. Common WD spectral types are summarized in table 1.4.

Table 1.4: Definition of white dwarf spectral types

Definition of Primary Spectral Symbols from McCook & Sion (1987)	
Spectral Type	Spectral Characteristics
DA	Only Balmer lines; no He I or metals present
DB	He I lines; no H or metals present
DC	Continuous spectrum, no lines deeper then 5% in any part of the electromagnetic spectrum
DZ	Metal lines only; no H or He lines
Additional Spectral Symbols	
Spectral Type	Spectral Characteristics
DAZ	Metal lines and H lines
DBZ	Metal lines and He lines

Most WDs, $\sim 80\%$ (Kepler et al., 2007; Vincent et al., 2024), have a hydrogen atmosphere (DA), which comprises $\sim$1% of their total mass (Dufour et al., 2010). This envelope of hydrogen is typically quite hot, with WD effective temperatures

ranging from $\sim 75,000$ K at the hot end (Bédard et al., 2020) to $< 4,000$ K at the low end (Hansen, 2004). The core of the WD emits as a blackbody, with the hydrogen atmosphere causing absorption features of the hydrogen Balmer series which are broadened due to the high surface gravity of the WD (Hansen, 2004). Other continuum opacity sources, such as collision induced absorption also contribute to the shape of the WD continuum in optical light (Kilic et al., 2006). While WDs likely form with non-DA spectral types, their high gravities result in gravitational separation and stratification of elements within the WD envelope.

1.2.1 White Dwarf Mixing Processes

WDs are extremely dense and have extreme surface gravities ($10^4 - 10^5$ times that of the Sun). Because of this, metals are sequestered deep in their atmospheres—becoming observationally inaccessible—on short timescales (days to $< 10^8$ yrs) (Zuckerman et al., 2003; Hansen, 2004; Schatzman, 1958; Fontaine & Michaud, 1979; Paquette et al., 1986). Diffusion due to gravity (i.e. "gravitational diffusion") is often assumed to be the dominant mechanism driving this sequestration of metals (Koester, 2009). Elements can diffuse through the envelope at different rates, due to differences in their masses and charges. Thus, different ionization states of the same element have different diffusion timescales (Bauer & Bildsten, 2019).

Convection

Convection occurs in the very outer layers of WDs with effective temperatures below $T_{eff} \approx 15,000$ K (Bauer & Bildsten, 2019). The mass exterior to the photosphere is also important when modeling mixing processes and timescales, so even for high

temperature WDs with no surface convection, a non-zero "convection zone mass" may be reported (Koester, 2009; Bauer & Bildsten, 2019). The convective WD hydrogen envelope has large-scale motions of material driven by a steep temperature gradient. Mixing timescales in the convective envelope are very short, and diffusion of heavy elements occurs at the base of the convective zone (Hansen, 2004). Other mixing processes can also come into play depending on the properties of the WD envelope.

Thermohaline Mixing

Thermohaline mixing (sometimes called "fingering convection") is another mixing process beyond the classic convection and gravitational diffusion. The accretion of heavy elements onto the surface of a WD creates a configuration where heavy elements decrease in concentration deeper into the radiative zone of the WD. This means that there is higher mean molecular weight material on top of lower mean molecular weight material. This unstable configuration allows thermohaline mixing to take effect, once a sufficient density ratio has built up (Deal et al., 2013). Thermohaline mixing requires the molecular weight gradient to be stable to convection, and the magnitude of both the thermal diffusivity and molecular weight gradient must be large enough that thermohaline instability is excited before particle diffusivity restabilizes the local composition (Bauer & Bildsten, 2019). Bauer & Bildsten (2019) note that there exists a regime of DAZ WDs for which their expected accretion rates are low enough that thermohaline mixing is not expected to be active. This threshold is temperature dependent, ranging from 10^{12} g s^{-1} for WD effective temperature of $6,000$ K to $< 10^{4}$ g s^{-1} for WD effective temperatures of $> 12,000$ K using Earth-composition accreted material. Published WD accretion rates in white dwarf - M

dwarf binaries range from $\sim 10^{-19} - 10^{-15}$ $M_\odot$ yr^{-1}, or $\sim 6 \times 10^6 - 6 \times 10^{10}$ g s^{-1}, and involve stellar composition accreted material.

Convective Overshoot

Convective overshoot is a mechanism that influences heavy element sequestration rates at the base of the convective zone (Tremblay et al., 2015). By extending the depth to which material is well-mixed, convective overshoot can increase the diffusion timescales, which are directly dependent on convective zone mass (Bauer & Bildsten, 2019). Bauer & Bildsten (2019) consider convective overshoot to be a possible explanation for diffusion timescales that are longer than predicted by models that only consider diffusion. However, they do not consider the effects of convective overshoot to be significant compared to the effects of thermohaline mixing above temperatures of $\sim 12,000$ K.

Significance of Mixing Processes

In summary, the regimes in which each of these mixing processes are significant are predominantly temperature dependent, other than gravitational diffusion. Below $\sim 10,000$ K, or in regimes of low accretion rate, thermohaline mixing is not a significant effect. However, models such as Bauer & Bildsten (2019) use planetary abundances for the accreted material. It is not clear whether thermohaline mixing is significant in regimes of higher accretion when the accreted material is only slightly enriched in metals, such as stellar abundance material. Convective overshoot is insignificant compared to thermohaline mixing above temperatures of $\sim 12,000$ K, though models such as Bauer & Bildsten (2019) do not include overshoot effects even below this

temperature regime due to quantitative uncertainty in its effects on mixing timescales. Convection occurs for DAs below 15,000 K, but convective zone mass fractions are still considered when modeling diffusion timescales of hotter WDs, by including the mass external to the photosphere. While not technically a mixing process, radiative levitation counters gravitational settling effects, and above 25,000 K can be strong enough to balance the effects of settling in WDs (Deal et al., 2013; Zuckerman et al., 2003).

1.2.2 White Dwarf Pollution

Metal lines are not expected in a white dwarf spectrum unless metal-rich material is being continuously added to its atmosphere (i.e. "accretion"). However, roughly one third of WDs show observed signatures of metal pollution, implying that they possess some continuous accretion source (Zuckerman et al., 2003). In the limit of WDs below 25,000 K, where radiative levitation can no longer explain the pollutants, 5-20% of DA and DB WDs show signs of metal pollution (Koester et al., 2005; Zuckerman et al., 2003; Deal et al., 2013). In the case of isolated WDs, an accretion disk or remnant planetary system is typically assumed to provide the reservoir for continuous accretion (Farihi et al., 2009; Farihi, 2016). Accretion disks emit at infrared wavelengths and thus can be detected spectroscopically or photometrically with broadband IR imaging by an infrared excess (Farihi, 2016). Remnant planetary systems becoming tidally disrupted are also often attributed to be the source of the accreting debris disks around isolated WDs, as seen in Vanderburg et al. (2015). However, in the case of WDs with a very close stellar companion, mass transfer can supply material to an accretion disk around the WD (Idan et al., 2008). Thus, WD pollution from an

accretion disk may have planetary or stellar elemental abundances depending on the source.

In the case of a close stellar companion, mass transfer can occur through a stellar wind. For a low mass stellar companion, this constitutes a low accretion regime onto the WD. In such cases, the accretion of wind material onto the WD can be used to constrain the wind mass-loss rate of the low mass stellar companion, as is done in D06 and W23. The regime in which wind accretion dominates is limited. Beyond separations of ~ 1 AU, the low mass stellar companion can perturb remnant planetary material onto the WD (Noor et al., 2024) and if the pair is too close, material from the outer layers of the low mass stellar companion become gravitationally bound to the WD, resulting in a mass transfer that dominates over the stellar wind (Eggleton, 1983).

1.3 Overview of M Dwarf - White Dwarf Binaries

White dwarf - M dwarf binaries (WD+MD) are gravitationally bound pairs containing a white dwarf primary and an M dwarf secondary. The white dwarf is assigned the primary by convention in white dwarf - main sequence pairs, because higher mass stars evolve off the main sequence faster than lower mass stars, suggesting that the WD progenitor was the higher mass star of the pair (Rebassa-Mansergas et al., 2010). For such a system, if the binary separation is small enough before the larger star evolves off the main sequence, the binary evolves through a common envelope phase in which the more massive star engulfs its companion during its red giant phase. This results in a rapid decrease of orbital period/binary separation, which contributes the energy and angular momentum that eventually ejects the common

envelope (Rebassa-Mansergas et al., 2016). One end result of the common envelope (CE) evolution is a post-common-envelope binary system (PCEB) containing a WD and a main sequence star (WD+MS). In this work, I am interested in PCEB systems containing a WD and an M dwarf. For systems with multiple observations, an orbital period can be estimated using changes in the radial velocities of the M dwarf and WD components. Systems with orbital periods under 300 days are considered PCEB systems (Rebassa-Mansergas et al., 2016).

These PCEB systems encompass the smallest separation fully detached pairs. They are also called pre-cataclysmic variable systems, because PCEB systems display orbital separation reduction over time. Eventually, these systems become close enough that the gravitational influence of the WD causes Roche lobe overflow of the M dwarf (mass transfer through the L1 Lagrange point, the point between two massive bodies at which their gravitational influence is balanced). This higher rate of mass transfer results in a cataclysmic variable (CV), typically defined as being a WD + Roche overfilling companion binary system (Carroll & Ostlie, 2017). Rebassa-Mansergas et al. (2016) define PCEB WD+MS systems to have orbital periods of less than 300 days. CVs tend to have orbital periods less than ~ 4 hours (Schreiber et al., 2024) but the maximum period a CV system can have depends on the parameters of the stars. The radius of the companion star and the mass ratio ($\frac{M_{companion}}{M_{WD}}$) determine this maximum period, with small companion radii and larger mass ratios decreasing the separation at which Roche overflow occurs. For PCEBs containing an M dwarf secondary, one can check whether the system is in the regime of Roche lobe overflow by comparing the radius of the M dwarf to the Roche radius, which defines the distance to which material is gravitationally bound to a star in a binary system (Eggleton,

1983).

Pollution of Companion White Dwarf

The final method of constraining wind mass-loss rates for M dwarf stars is to use WD+MD binaries. Close but fully detached PCEB WD+MD binaries provide an excellent method of constraining the M dwarf wind by quantifying the pollution of the WD envelope due to the continuous accretion of M dwarf wind material. While both wide WD+MD binaries (separation $\sim 1 - 160$ AU) and PCEB binaries (separation $\sim 0.001 - 0.02$ AU) were used in D06, stellar wind pollution is not thought to be the cause of accretion in the widest two pairs, WD 1210+464 and WD 1049+103. Notably, WD 0354+463, which was classified as a wide binary in D06 was instead considered a PCEB by W23, after binary orbit characterization by Ashley et al. (2019) where the orbital period of WD 0354+463 was found to be 0.165 days. The ten WD+MD binaries with wind mass-loss rates determined using the WD pollution methodology are shown in table 1.5. Other papers such as Tappert et al. (2011b); Parsons et al. (2012); Pyrzas et al. (2012); Ribeiro et al. (2013) and W23 use similar methodology to D06, though Tappert et al. (2011b); Parsons et al. (2012); Pyrzas et al. (2012) and Ribeiro et al. (2013) provide white dwarf accretion rates rather than M dwarf wind mass-loss rates. The WD accretion rate is the rate at which material would have to be added to the WD to result in the detected absorption features. If all the wind material lost from the M dwarf is accreted onto the WD, then the WD accretion rate and M dwarf mass loss rate would be equal, but in most cases the WD accretion rate acts as a lower limit to the M dwarf wind rate.

I am interested in PCEB systems also because WD+MD pairs that are too widely

separated ($\gtrsim$ 1 AU) may exhibit WD pollution due to other effects than pure wind accretion (D06) such as the accretion of a remnant planetary system. The common-envelope phase of PCEB systems clears out planetary material out to $\sim$ 3 AU, and the $<$ 1 AU separations of PCEB systems are not likely to perturb remnant planetary material beyond $\sim$ 3 AU (Villaver & Livio, 2007). In D06 the wide binaries were found to require M dwarf wind mass-loss rates greater than 10^{-11} $M_{\odot}yr^{-1}$ and the author concluded that the wind values were unrealistic for the wide binary systems, stating that wind accretion alone could not account for the total pollution seen in wide binary DAZs with low mass companions. It is likely that the excess pollution seen in wide binary WD+MD pairs comes from the accretion of a remnant planetary system onto the WD (Noor et al., 2024). However, this is not likely to affect close ($<$ 1 AU) WD+MD binary systems, because the planetary nebula phase of WD evolution clears out planets within $\sim$ 3 AU of the WD (Villaver & Livio, 2007). While a wide M dwarf companion could perturb remnant planetary debris towards the WD from greater distances where planetary material survived, this is not likely to occur in the close binary systems. Therefore, we can assume the M dwarf stellar wind is the only source of WD pollution in close WD+MD binary systems. The close binaries were found to require winds on the order of 10^{-16} to 10^{-15} $M_{\odot}$ yr^{-1}. For comparison, the Sun's wind mass-loss rate is $\sim 2 \times 10^{-14}$ $M_{\odot}$ yr^{-1} (Parker, 1958).

In the case of a close but fully detached binary pair containing a WD and an M dwarf, the stellar wind of the M dwarf can provide an accretion source resulting in WD photospheric pollution (D06). The accretion rate onto the WD can be calculated from the abundance of metal polluting its spectrum. When combined with knowledge of the separation of the WD+MD binary, the M dwarf mass-loss rate can be calculated

(D06). This methodology is described in section 2.2. The bulk composition of the accreted wind material is often assumed to be solar (D06; W23), in contrast to the Earth-like pollutant compositions that are expected for isolated WDs.

Figure 1.1 details the M dwarf wind mass-loss rates of all the systems discussed thus far across the four methodologies. The Sun's wind rate is shown for scale. Of the existing M dwarf wind mass-loss rate estimates, the largest are roughly three orders of magnitude larger than the Sun's wind rate, and the smallest are nearly three orders of magnitude smaller than the Sun's wind rate.

Table 1.5: M dwarf wind mass-loss rates for the ten systems where the wind rates were determined using the WD pollution method. The winds from all methods are compiled in table A.1.
References: (1) D06 (2) W23

WD Companion Pollution Wind Rates			
Star Name	Mass ($M_\odot$) or Spectral Type	Wind Mass-Loss Rate ($M_\odot$ / yr)	Ref.
WD 0419-487	0.095	6×10^{-15}	1
LHS 1660 (WD 0419-487)	M5	9.9×10^{-15} - 3.2×10^{-13}	2
WD 1026+002	0.23	10^{-16}	1
PG 1026+002 (WD 1026+002)	M5	4.4×10^{-16} - 2×10^{-14}	2
WD 1213+528	0.36	10^{-16}	1
Case 1 (WD 1213+528)	M3	1.9×10^{-15} - 10^{-13}	2
WD 0354+463	unknown	6×10^{-10}	1
Rubin 80 (WD 0354+463)	M7	10^{-14} - 3.7×10^{-13}	2
WD 1049+103	unknown	7×10^{-10}	1
WD 1210+464	unknown	5×10^{-8}	1
LTT 560	M6	9.4×10^{-14} - 3.1×10^{-12}	2
PG 2257+162	M5	1.3×10^{-16} - 3.2×10^{-15}	2
BPM 6502	M5	2.6×10^{-16} - 1.3×10^{-14}	2
GD 448	M7	7.0×10^{-17} - 1.9×10^{-15}	2

1.3.1 PCEBs and enhanced wind rates

In this thesis, I use the WD+MD methodology for constraining M dwarf wind mass-loss rates using the pollution of a WD companion. All of the systems analyzed in this work have gone through a common envelope phase, as their orbital periods are all below 12.5 days and the upper limit for PCEB orbital periods is 300 days according to Rebassa-Mansergas et al. (2016). Magnetically active stars can be identified by the presence of the spectral emission lines, such as Hα, which is magnetically sensitive. All M dwarfs in the 63 PCEB systems analyzed by Rebassa-Mansergas et al. (2013) were found to be magnetically active. Magnetic activity was determined by subtracting the best WD model fit from the WD+MD SDSS spectrum, normalizing the spectrum using a parabolic fit to the local continuum in the Hα region, and calculating the Hα EW and EW uncertainty. Their requirements were that active M dwarfs had an Hα emission line with EW magnitude greater than 0.75 Angstroms (Å) (by convention, emission lines have negative EW) and EW magnitude greater than three times the EW uncertainty. West et al. (2011) also classifies M dwarf stars as magnetically active in Hα at an equivalent width threshold of 0.75 Å. Note that West et al. (2011) use equivalent width signs opposite to convention, so this is referring to an emission line of equivalent width 0.75 Å (typically written -0.75 Å). Rebassa-Mansergas et al. (2013) estimated the influence of irradiation effects for 47 PCEB systems (for which orbital periods and stellar parameters were well constrained) since Hα emission can also be caused by the irradiation of the M dwarf by a hot WD companion, or if the orbital period is very short (Tappert et al., 2011a,b). Rebassa-Mansergas et al. (2013) expect that $\sim$ 93% of their sample are not affected by irradiation, and conclude that all M dwarfs in PCEB systems are magnetically active. It should be noted, however, that

many M dwarfs show different amounts of magnetic activity at different times. Both short and long term variability have been observed, with short-term variability of emission lines typically < 200 days (Mignon et al., 2023). Comparing two spectra of SDSS J164615.60+422349.2 in figure 1.2 we see that the Hα and Ca II H&K emission are significantly different.

Since stellar winds are magnetically driven, magnetic activity is expected to influence the M dwarf's stellar wind mass-loss rate. As seen in the slingshot prominence method for constraining M dwarf winds (section 1.1.1), very active and rapidly rotating M dwarfs sometimes have higher wind rates than those determined by other methods, such as the astrosphere method. However, if all M dwarfs in PCEB systems are indeed magnetically active they do not seem to display the same extreme wind rates as slingshot prominence stars. Indeed, some of the lowest constrained M dwarf wind rates have been found using WD pollution in PCEB systems. PCEB are therefore well suited to expanding our understanding of wind rates. Though M dwarfs in PCEB systems may not perfectly mimic the properties of field stars (in terms of their magnetic evolution), they may help us learn about the wind properties in young/magnetically active M dwarfs. M dwarf behaviour during the early times of their planetary system formation is important to understanding the planet formation process around M dwarf stars and early atmosphere evolution of these planets.

The WD being magnetically active is important to how much of the wind material is accreted, with W23 claiming that very magnetic WDs can couple to the field lines of the M dwarf, accreting all of the lost material from the M dwarf wind out to several $R_\odot$. If this were the case, standard accretion models such as Bondi-Hoyle-Lyttleton accretion would underestimate the fraction of wind material being accreted by the

WD, resulting in an overestimation of the calculated M dwarf mass-loss rate. However, determining magnetic activity for accreting WDs is usually done by identifying cyclotron emission using phase folded light curves (van Roestel et al., 2025), which is beyond the scope of this work.

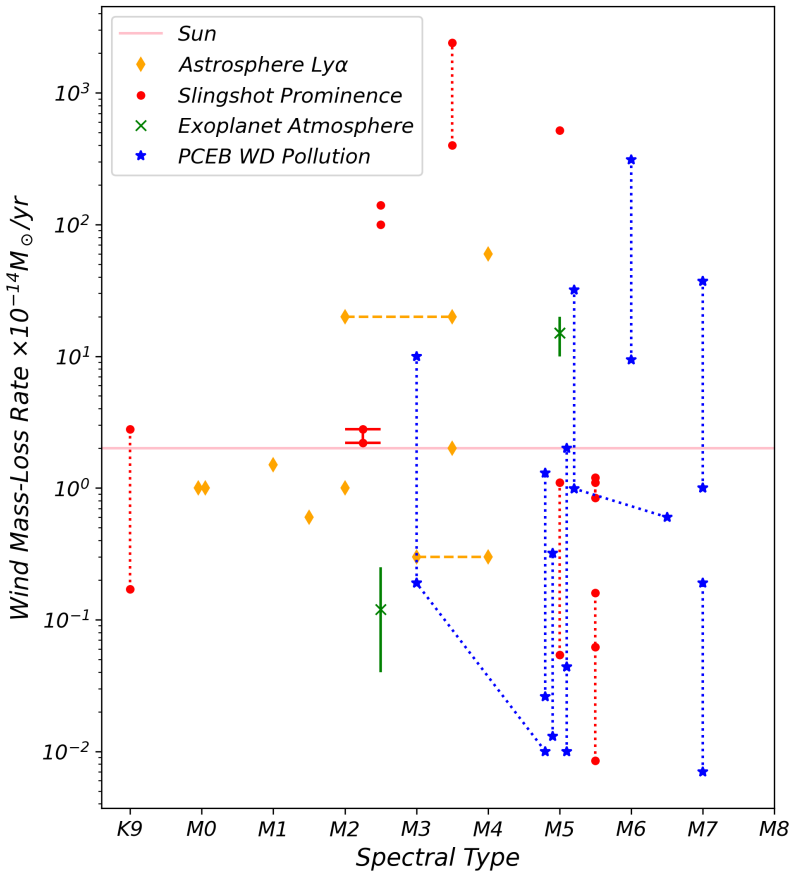

Figure 1.1: M dwarf wind mass-loss rates of the systems discussed thus far. The Sun's rate is shown as a pink horizontal line for scale. Stars with multiple reported mass-loss rates have the multiple rates connected by a dotted line. Sometimes a star is assigned different spectral types in different publications. Stars for which mass was reported instead of spectral type were assigned a spectral type based on the closest mass match in "A Modern Mean Dwarf Stellar Color and Effective Temperature Sequence" (Pecaut & Mamajek, 2013). AD Leo has spectral type error bars due to a reported mass equidistant from spectral types M2 and M2.5. The Astrosphere Lyα systems are orange diamonds, with binary systems connected by horizontal dashed lines. Binary system wind rates represent the combined total wind rate of both stars. Slingshot Prominence systems are red circles. Exoplanet Atmosphere Loss systems are green crosses with solid line error bars. AU Mic only provided a range for mass-loss rate, so the mean was assigned. PCEB WD Pollution systems are blue stars. The wide binary systems from D06 are excluded from this plot, since it is unlikely that the M dwarf wind is the sole cause of WD pollution in wide binary systems.

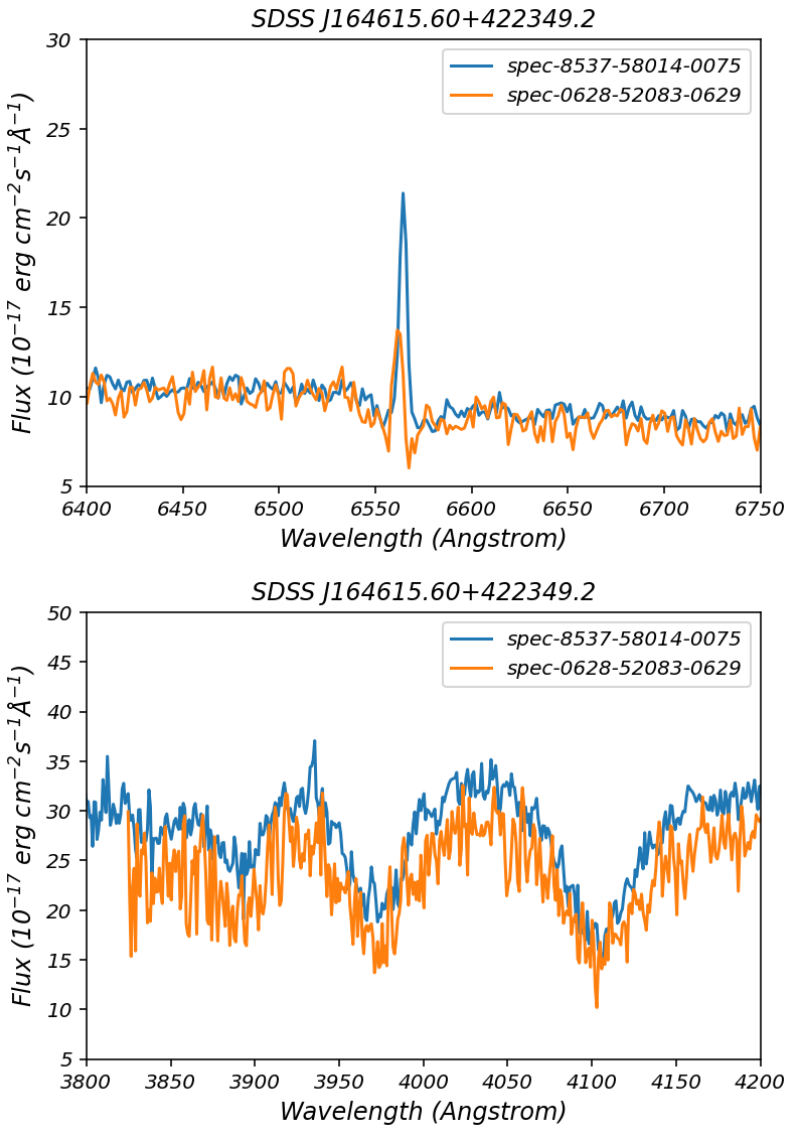

Figure 1.2: Comparison of magnetically sensitive emission lines in SDSS J164615.60+422349.2 from two different SDSS spectra taken roughly 16 years apart. The blue spectrum was observed on September 18, 2017 and the orange spectrum was observed on June 23, 2001. Upper: a close-up of the Hα region. Lower: a close-up of the Ca II H&K region.

Chapter 2

Methodology

M dwarf winds are poorly constrained and poorly understood. Due to the difficulty of observing them, very few measurements exist. Additionally, upper limits of M dwarf wind mass-loss rates using methodologies such as the radio emission method tend to be orders of magnitude larger than the Sun's wind mass-loss rate. These upper limits are similar to the wind mass-loss rates found for very active M dwarfs and provide little insight into the true distribution of wind mass-loss rates of typical M dwarf stars. There are a few key advantages to constraining M dwarf winds using a nearby WD companion. In the past, this methodology has only been used in situations where the WD shows clear signs of metal pollution, and sometimes only to determine the rate of accretion onto the WD, rather than the mass-loss rate of the M dwarf. However, non-detections can provide useful information to calculate M dwarf wind upper limits. The relatively low wind rates calculated for PCEB WD+MD pairs in previous works suggested that non-detections in these systems would provide more conservative upper limits than other methodologies (Debes, 2006; Walters et al., 2023). Many WD+MD

binaries have been observed unintentionally by SDSS due to overlapping in colour-colour space with quasars (Rebassa-Mansergas et al., 2016), providing hundreds to thousands of systems that could yield M dwarf wind constraints.

In this work, I consider 90 WD+MD systems, selecting those with favourable system parameters for constraining M dwarf wind mass-loss rates. While previous works using similar methodology to ours have required clear signs of WD metal pollution to constrain M dwarf wind rates, I compile one sample with the visible WD pollution constraint, and four additional samples without this requirement.

2.1 The Data

The spectra used in this work come from the Sloan Digital Sky Survey (SDSS), because there exist catalogues of WD+MD binaries with available SDSS spectra and previously determined parameters, such as orbital period, that are crucial for wind rate calculations (D06). Additionally, SDSS spectra cover a sufficient wavelength regime such that the Ca II H&K lines are included, and introduce minimal spectral distortion such that spectral contributions of the WD and M dwarf can be disentangled. SDSS uses a dedicated 2.5 m wide-angle optical telescope located at the Apache Point Observatory in New Mexico, United States. This telescope has been involved in all data releases (DR) to date (DR19). The original instruments used to observe were a multi-object/multi-fiber spectrograph and a multi-filter/multi-array CCD camera. New spectrographs have been introduced, but the original instruments are no longer operational. SDSS used a photometric system of five filters, ugriz, to identify the nature of the targets (star, galaxy, quasar, etc), and select targets for spectroscopy. The specific steps to the identification pipeline change regularly, between the various

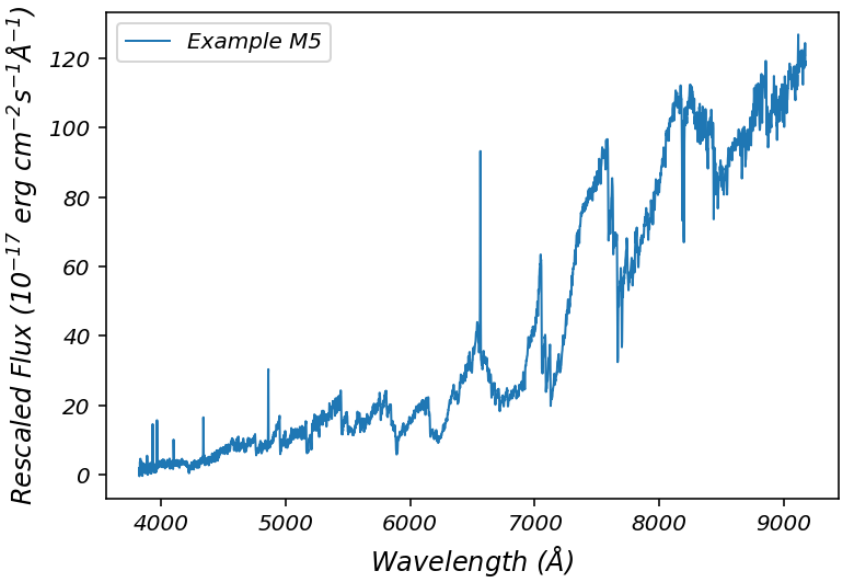

Figure 2.1: An example spectrum of a magnetically active M5 star from the Sloan Digital Sky Survey Data Release 7 Spectroscopic M Dwarf Catalogue (West et al., 2011). The spectrum has been rescaled such that the flux around 8350 Å is 100×10^{-17}erg cm^{-2}s^{-1}Å^{-1}

data releases of SDSS. An overview of the processing, pipelines, and data products can be found in the SDSS Early Data Release (EDR) paper (Stoughton et al., 2002).

Specifically, the data I use come from Data Releases 7, and 9-12. Data Release 7 has spectroscopic wavelength coverage of 3800-9200 Å, with resolution ranging from R∼1800 (blue end) to R∼2200 (red end). From Data Release 7, I use 192 M dwarf spectra from the Sloan Digital Sky Survey Data Release 7 Spectroscopic M Dwarf Catalogue (West et al., 2011). These spectra are used to create templates of magnetically active M dwarfs, which I use to calculate the M dwarf Ca emission contributions for my WD+MD targets. An example M dwarf spectrum is shown in figure 2.1.

Data Releases 9 through 12 have spectroscopic wavelength coverage of 3600-10,400

Å, with resolution ranging from R∼1300 (blue end) to R∼3000 (red end). I use unresolved spectra from 90 systems in the Sloan Digital Sky Survey White Dwarf Main Sequence (SDSS WDMS) binary catalogue (Rebassa-Mansergas et al., 2012) which consist of spectra from SDSS DR9-DR12.

Images of galaxies and stars differentiated based on morphology, described in section 4.4.6 in Stoughton et al. (2002). Galaxy target selection also uses a variety of magnitude cuts, described in section 4.8.1 in Stoughton et al. (2002), resulting in a sample that is contaminated at the $\sim 1\%$ level by close binary stars that cannot be deblended. Quasars are selected based on their colours, which are distinct from normal stars, and have a efficiency slightly less than 65% in Stoughton et al. (2002). Stars are also targeted by their colours, and though the sample is incomplete, there are several thousand spectra available as of the SDSS EDR for stars of all spectral types.

There have been many phases of SDSS, with different surveys focusing on different scientific questions. SDSS has been interested in obtaining spectra of galaxies and quasars, exploring the structure and stellar makeup of the Milky Way, large-scale structure of the Universe, the expansion rate of the Universe, etc. Interestingly, the majority of white dwarf-main sequence binaries observed by SDSS were not observed intentionally. White dwarf-main sequence binaries overlap in colour space with quasars (Smolčić et al., 2004), so many of them were targeted as quasars in SDSS Surveys (Rebassa-Mansergas et al., 2016). However, not all WD+MS systems are observed by mistake. Rebassa-Mansergas et al. (2012) intentionally targeted WD+MS binaries in their dedicated survey, for example.

2.2 Sample Selection

I defined five samples of M dwarf - white dwarf systems that are suitable for studying M dwarf winds. Each of these samples are derived from the SDSS WDMS binary catalogue (Rebassa-Mansergas et al., 2012). The SDSS WDMS binary catalogue is a data base containing over 3200 white dwarf-main sequence binaries identified within SDSS (Rebassa-Mansergas et al., 2012). From the SDSS WDMS binary catalogue, I selected only the targets with known orbital period, and secondary star mass below 0.6 solar masses, resulting in 90 systems. This was done to ensure I am only considering WD-M dwarf binaries that I can calculate separations for, since the pair separation is crucial to calculating the M dwarf wind rate. Within this sample, an orbital period, SDSS name, binary type, coordinates, and ugriz magnitudes are provided for every system. Other important parameters including WD effective temperature, WD surface gravity, WD mass, WD radius, WD distance, M dwarf distance, M dwarf spectral type, M dwarf mass, M dwarf radius, M dwarf distance, and other magnitudes (near-ultraviolet, far-ultraviolet, and a set of near-infrared bands YJHK) are provided for most systems. Note that the WD distance and M dwarf distance do not always agree, and Gaia DR3 distances often do not agree with either the WD distance or M dwarf distance reported in the SDSS WDMS catalogue. Rebassa-Mansergas et al. (2007) independently estimated the WD and M dwarf distances from the flux scaling factors of the WD models and M dwarf templates they used (please see section 3.5 of Rebassa-Mansergas et al. (2007) for the details). Additionally, I was not able to recover reasonable flux scaling factors to match the WD model flux to the observed flux from the WD distance and radius values, despite using the same grid of WD models as Rebassa-Mansergas et al. (2007) (see section 2.2.2). For these reasons, I

opted to not use the reported WD or M dwarf distances to scale the Koester (2010) WD models in this work. Instead, I determine a model scale factor for each system as described in section 2.2.2.

From this dataset, I identify the white dwarfs most likely to exhibit metal absorption features, while still being in the regime where stellar wind is the dominant mass transfer mechanism (i.e. "wind-dominated regime").

First Check: Wind-Dominated Regime

The first step, which I applied to all five samples, was to check each system to ensure the M dwarf secondary was not overfilling its Roche lobe. To determine whether a WD with a close stellar companion is accreting material due to the companion overfilling its Roche lobe, the Eggleton equation may be used (Eggleton, 1983). The Eggleton equation calculates a Roche radius,

$$R_{Roche} = a\frac{0.49q^{2/3}}{0.6q^{2/3} + ln(1+q^{1/3})}, \tag{2.2.1}$$

where a is the separation of the binary and q is the mass ratio of the two stars, with the star for which the Roche radius is being calculated in the numerator. When checking if the companion star is overfilling its Roche lobe, the mass ratio is $q = \frac{M_{companion}}{M_{WD}}$. The Roche lobe effective radius may then be compared to the radius of the companion star to determine if the system is in the wind-dominated regime. Only the M dwarf needs to be tested in this way, as there is no scenario in which a WD is overfilling its Roche lobe while its main-sequence companion is not. This is due to the compactness of WDs; the separation at which a WD overfills its Roche lobe is much smaller than the separation at which the main-sequence companion begins overfilling

its Roche lobe. The Eggleton equation approximates the Roche lobe effective radius to "better than 1%" (Eggleton, 1983) for $0 < q < \infty$. This calculation depends on the WD mass, the M dwarf mass, the pair separation, and the M dwarf radius.

The SDSS WDMS catalogue provided WD masses for 76 of the 90 systems, which were found (Rebassa-Mansergas et al., 2016) using the spectral decomposition and fitting technique described in section 3 of Rebassa-Mansergas et al. (2007), but using the updated Koester (2010) model grid, instead of the Koester et al. (2005) model grid. I use the Koester (2010) model grid as well, with the best-fit WD surface gravity and effective temperature. An example best-fit Koester model is shown in figure 2.2. After Rebassa-Mansergas et al. (2016) determine and scale the best-fit M dwarf template, the M dwarf template is subtracted from the combined spectrum. The normalized Balmer lines of the residual WD spectrum is fitted with the Koester (2010) grid of DA models to determine effective temperature and surface gravity. The entire residual WD spectrum (continuum plus lines) is also fitted to break the 'hot/cold solution degeneracy' that can occur when just the Balmer lines are fitted. The hot/cold degeneracy occurs because the same lines can be fit well with two WD effective temperature and surface gravity combinations, one above and one below $T_{eff} \sim 13,000$ K. Additionally, Rebassa-Mansergas et al. (2016) apply 3D corrections from Tremblay et al. (2013) to their surface gravity and effective temperature determinations, as the DA model spectra they used overestimate surface gravities for cool ($< 12,000$ K) WD. WD masses are then determined using interpolated cooling sequences from Bergeron et al. (1995). For the 14 systems for which a WD mass was not determined by Rebassa-Mansergas et al. (2016), I assumed a WD mass of 0.6 $\pm$0.1 $M_{\odot}$. This assumption was made because the distribution of DA masses peaks sharply at 0.6

$M_{\odot}$ (Hansen, 2004; Kepler et al., 2007), with the majority having masses between 0.5 and 0.7 $M_{\odot}$ (Kepler et al., 2007). All of the systems that were missing a WD mass were also missing the WD surface gravity, effective temperature, and radius. However, four of the systems that were missing WD information had WD surface gravity and effective temperature reported in Morgan et al. (2012), which I adopted. These systems were: SDSS J030308.35+005444.1, SDSS J030716.44+384822.8, SDSS J085336.03+072033.5, and SDSS J231105.66+220208.6. Of the 14 systems for which I assumed a WD mass of 0.6 $\pm$0.1 $M_{\odot}$, only two systems, SDSS J030716.44+384822.8 and SDSS J231105.66+220208.6 made it into my final sample.

The SDSS WDMS catalogue provided M dwarf spectral types for 83 of the 90 systems. As before, the spectral decomposition and fitting technique described in section 3 of Rebassa-Mansergas et al. (2007) is used, with a combined set of observed M dwarf and white dwarf templates (different than the WD models used to determine WD properties discussed above). Notably, where multiple spectra for a single target are available, Rebassa-Mansergas et al. (2016) average the parameter values of the individual fits. For this reason, the secondary spectral types for SDSS J172406.14+562003.0 and SDSS J022503.02+005456.2 are nonstandard values of 3.33 and 4.4, respectively. All other M dwarf spectral types provided by Rebassa-Mansergas et al. (2016) are half-integer spectral types from M0V to M9.5V. Two of the systems missing M dwarf spectral type information had spectral types reported in Morgan et al. (2012). These systems were SDSS J220848.99+122144.7 and SDSS J223530.61+142855.0, which do not overlap with the systems I adopted WD values from Morgan et al. (2012) for. I adopted the Morgan et al. (2012) M dwarf spectral type values for these systems. From the spectral types, which are stated to have an

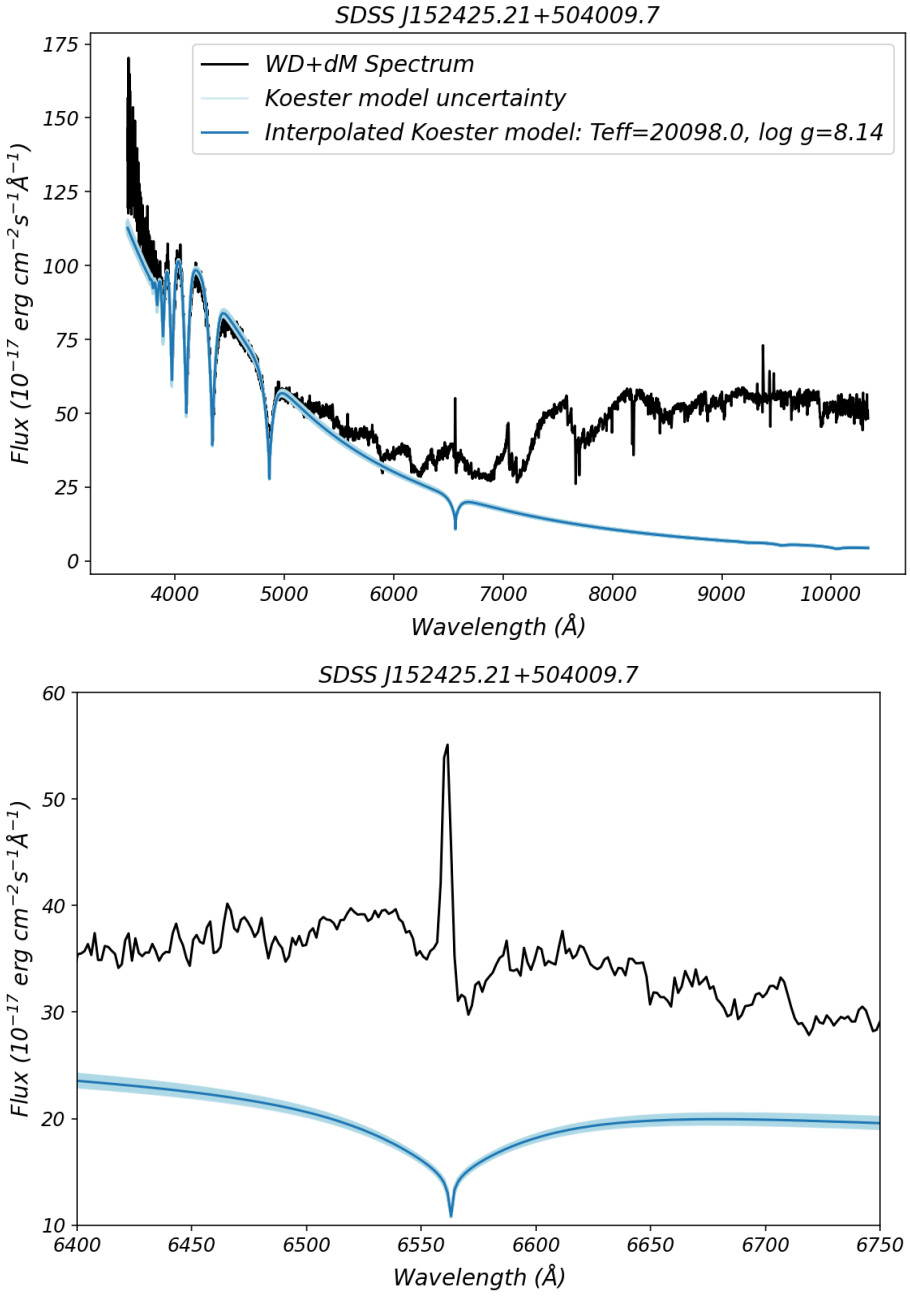

Figure 2.2: Upper: an example best-fit scaled Koester model (dark blue) and resamples (light blue) within WD effective temperature and surface gravity uncertainties overlaid on the WD+MD SDSS spectrum (black). Lower: a closer look at the Hα region where the model uncertainties are more visible.

uncertainty of ± 0.5, an empirical spectral type-radius relation from compiled literature values is used to determine the radius (Rebassa-Mansergas et al., 2007). There were relatively few systems used to define this relation and a large amount of scatter, with radii of $\sim 0.1 - 0.7\ R_{\odot}$ at spectral type M5V. An empirical spectral type-mass relation was also used in Rebassa-Mansergas et al. (2007) from compiled literature values. I opted to not use these M dwarf mass and radius values, due to the large uncertainties, and systematic offset compared to the more recent values found using Pecaut & Mamajek (2013). This also provides the benefit of internal consistency in how M dwarf masses and radii are obtained for the systems with M dwarf spectral type adopted from Morgan et al. (2012). I use "A Modern Mean Dwarf Stellar Color and Effective Temperature Sequence" version 2022.04.16 (Pecaut & Mamajek, 2013) to determine mass and radius values for the M dwarf stars. Uncertainties on these masses and radii were determined by taking the average of the absolute difference between the masses and radii that would be assigned by one half spectral type above or below the best fit value. For M0V and M9.5V stars, the absolute difference between the mass and radius assigned by the best fit spectral type and the mass and radius assigned by the bounding spectral type (M0.5V and M9V, respectively) were used instead. For both these cases, the resultant mass and radius uncertainties are greater than or equal to the uncertainties that would be assigned if the other bounding spectral types (K9V and L0V) were used.

All 90 systems had orbital period values reported, as this was a condition on my initial selection. The binary separations are obtained using the reported orbital periods, obtained in Rebassa-Mansergas et al. (2016) using Scargle (1982) periodograms

calculated from the radial velocities of each system to determine the most likely period. I recovered orbital separations using Kepler's third law for the 83 systems with available half-integer M dwarf spectral types.

$$a = \left(\frac{G(M_{WD} + M_{MD})}{4\pi^2}\right)^{1/3} p_{orb}^{2/3} \tag{2.2.2}$$

Where p_{orb} is the orbital period, M_{WD} is the mass of the WD, and M_{MD} is the mass of the M dwarf. The two systems with non-half-integer spectral types, SDSS J172406.14+562003.0 and SDSS J022503.02+005456.2, were not included among the 83 systems. SDSS J022503.02+005456.2 was excluded because it was also missing the WD information, and SDSS J172406.14+562003.0 because its WD was far too hot, and would have been discarded from all samples at a later stage in the target selection.

With these parameters, I was able to confirm which systems should be in the wind-dominated regime (no Roche overflow). From my starting sample of 90 systems, I was able to calculate the Roche radius for 83 of them. For each system, I recalculated the M dwarf radius and Roche radius 50,000 times using system parameters resampled independently from Gaussian distributions using numpy.random.normal(). Of the 83 systems for which the Roche radius could be calculated, 73 are not overfilling their Roche lobe after applying a $> 95\%$ confidence condition.

Second Check: Expected Detectable WD Metal Pollution

Next, I check whether detectable absorption signatures of pollutants in the WD photosphere are expected. This is done for all possible systems, regardless of if they are expected to be experiencing Roche overflow, but is only used in defining 3 of my 5

samples. I was interested, specifically, in calcium absorption in white dwarf spectra. Calcium produces strong absorption features in visible light, the Ca H&K lines at 3933.663 and 3968.469 Å (Johnson et al., 2022), typically the strongest and most common metal absorption features in optical spectra of polluted WDs (Zuckerman et al., 2003; Hansen, 2004; Debes, 2006). The calcium H line at 3968.469 Å overlaps with the broad hydrogen absorption feature at 3970.1 Å in WD spectra, so the calcium K line is used in this work.

D06 related the WD abundance of calcium to the bulk accretion rate of the WD by assuming the accreted material was of Solar composition, and assuming the WD accretes through Bondi-Hoyle-Lyttleton (BHL) accretion. The BHL accretion model describes the spherically symmetric accretion of material onto a compact object moving through a uniform medium (Bondi, 1952; Bondi & Hoyle, 1944; Lyttleton, 1972). It simplifies our view of wind accretion by assuming the WD is a point-like accretor, and that the stellar wind from the companion is uniform, ignoring interactions the wind may have with magnetic fields. The BHL accretion rate is

$$\dot{M}_{WD} = \frac{4\pi G^2 M_{WD}^2 \rho(a)}{v_{rel}^3}, \tag{2.2.3}$$

where G is the gravitational constant, $\rho(a)$ is the density of the wind material at the location of the WD, v_{rel} is the relative velocity of the WD with respect to the wind material (taken to be $\sqrt{v_{wind}^2 + v_{orb}^2}$) where v_{wind} is the escape velocity at the surface of the M dwarf and v_{orb} is the orbital velocity of the binary.

D06 assumes an M dwarf wind that is spherically symmetric, and leaves the M dwarf at the escape velocity with a constant mass-loss rate. They describe the wind

material density using the continuity equation of Lamers & Cassinelli (1999):

$$\rho(a) = \frac{\dot{M}_{MD}}{4\pi v_{rel} a^2}, \tag{2.2.4}$$

where $\dot{M}_{MD}$ is the total mass-loss rate of the wind material from the M dwarf, v_{rel} is the relative velocity as defined before, and a is the distance from the M dwarf at which the density is being evaluated (the location of the WD). The simplifications D06 implements ignore potential mechanisms which could suppress or enhance the BHL accretion rate. For example, a WD with strong magnetic fields can accrete wind material more efficiently than the BHL model predicts resulting in overestimated M dwarf wind mass-loss rates (Li et al., 1994). Conversely, simulations have shown wind accretion to be less efficient than predicted by BHL when $v_{orb} \approx v_{wind}$ (Theuns et al., 1996; Liu et al., 2017), which would result in under-predicted M dwarf wind mass-loss rates.

Combining the BHL equation and the wind density equation, and assuming the WD has been accreting Solar composition material for long enough to have reached steady state accretion, D06 derive an equation to determine the M dwarf wind mass-loss rate from the WD calcium abundance. The diffusion timescale of calcium in the WD is equal to the accretion rate of calcium when the system is in equilibrium. Equilibrium is typically assumed due to the short diffusion timescales in WDs relative to their ages (Bauer & Bildsten, 2019). I adapt this equation to instead calculate an expected WD calcium abundance using an assumed M dwarf wind mass-loss rate

$$\mathrm{Ca/H} = (\dot{M}_{MD} M_{WD} \Theta G^2)/(q_{conv} a^2 v_{rel}^4 (\mathrm{Ca/H})_{\odot}), \tag{2.2.5}$$

where Ca/H is the calculated calcium abundance in the form N(Ca)/N(H), M_{WD} is the white dwarf mass, $\dot{M}_{MD}$ is the assumed M dwarf mass-loss rate, Θ is the diffusion timescale of calcium in the white dwarf atmosphere, G is the gravitational constant, q_{conv} is the white dwarf convective zone mass fraction, a is the separation of the binary, v_{rel} is the relative velocity of the white dwarf with respect to the wind material, and $(\mathrm{Ca/H})_{\odot}$ is the Solar calcium abundance, for which I use the same value as D06, $(\mathrm{Ca/H})_{\odot} = 2.1875 \times 10^{-6}$ (Asplund et al., 2009). For comparison against detectability thresholds, I take the logarithm of Ca/H such that our calcium abundance is of the form log (N(Ca)/N(H)), as these are the values typically reported in literature.

This test is done to ensure that I am looking at systems for which detectable calcium pollution in the WD is expected. I do not want to limit my analysis only to the systems with visible calcium absorption, especially because I expect that meaningful upper limits can be obtained for non-detections. Additionally, even though there end up being M dwarf calcium emission lines in many ($\sim$ 40) of these systems, it is useful to know which ones are expected to have detectable calcium pollution in the event that absorption features are detectable at a different points in time as seen with SDSS J164615.60+422349.2. This system has two SDSS spectra taken at different times with one spectrum showing WD calcium absorption and one spectrum not showing WD calcium absorption. The different calcium signatures for SDSS J164615.60+422349.2 can be seen in the lower panel of figure 1.2.

From my starting sample of 90 systems, I was able to calculate the expected WD calcium abundance for 74 of them. This calculation depends on WD mass, WD

effective temperature, separation, relative velocity, and an assumed M dwarf mass-loss rate. WD mass and effective temperature values were missing from 14 of the 90 systems, for which 4 had WD effective temperatures reported in Morgan et al. (2012) that I adopted, and I assumed a WD mass of $0.6 \pm 0.1 M_{\odot}$. Of the remaining 80 systems, separations could only be calculated for 74 of them, due to the 5 which were missing M dwarf spectral types in both Rebassa-Mansergas et al. (2012) and Morgan et al. (2012), and the one with a nonstandard spectral type and WD effective temperature too hot to be retained in later selection cuts.

The relative velocities are not reported directly in the SDSS WDMS binary catalogue, but I calculate them using the orbital velocities, and assuming a wind speed equal to the escape speed of the M dwarf. The orbital velocities are calculated by assuming circular orbits and the velocity equation for circular motion:

$$v_{orb} = \frac{2\pi a}{p_{orb}}, \tag{2.2.6}$$

where a is the separation and p_{orb} is the orbital period.

The escape velocity is calculated using the mass and radius of the M dwarf:

$$v_{esc} = \sqrt{\frac{2GM_{MD}}{R_{MD}}}, \tag{2.2.7}$$

where M_{MD} is the mass of the M dwarf and R_{MD} is the radius of the M dwarf.

I adopt the same assumption as D06 for calculating the relative velocity:

$$v_{rel} = \sqrt{v_{orb}^2 + v_{esc}^2} \tag{2.2.8}$$

Our relative velocities range from $\sim 560 - 750$ km/s, with relative uncertainties ranging from $\sim 1 - 10\%$. These are in agreement with the relative velocities in D06 which were $\sim 600 - 650$ km/s and assumed $M_{MD}/R_{MD} \sim 1$.

The e-folding timescale of calcium (Θ) describes how long it takes for calcium to settle out of the atmosphere of a WD, depending on the WD surface gravity, density, and convective zone mass fraction. The convective zone mass fraction is the fraction of the WD mass above the radiative zone, and depends on the WD mass and effective temperature. I use the e-folding timescales and convective zone mass fractions of Bauer & Bildsten (2019), which implement more recent coefficients for ionic transport in dense plasmas in their diffusion calculations, and have the benefit of internal consistency in the the physics used to determine both parameters. The Bauer & Bildsten (2019) diffusion timescales of calcium, and WD convective zone mass fractions are obtained from (1D) white dwarf atmosphere models computed with the stellar evolution code 'Modules for Experiments in Stellar Astrophysics' (MESA) (Paxton et al., 2011, 2013, 2015, 2018, 2019; Jermyn et al., 2023). MESA is an open-source, 1D stellar evolution code, primarily written in Fortran. Bauer & Bildsten (2019) use MESA version 10398 for their diffusion models, which are the models that generated the tables I use. The tables provide diffusion timescales and convective zone mass fractions based on the mass and temperature of the white dwarf. These models assume that no other mixing occurs below the convective zone and that gravitational sedimentation is the only diffusion mechanism, so additional mixing processes such as thermohaline mixing are not included (Bauer & Bildsten, 2019). These models are computed using the coefficients of Stanton & Murillo (2016) for ionic transport in dense plasmas. The tables span the temperature range from 6,000 K to

20,500 K, in steps of 500 K. The three WD mass values considered are 0.38 $M_{\odot}$, 0.6 $M_{\odot}$, and 0.9 $M_{\odot}$. I interpolate these tables linearly (using RegularGridInterpolator from scipy.interpolate), and extrapolate beyond the upper temperature and mass bounds. I accept extrapolated values up to a WD mass of 1.1 $M_{\odot}$ and temperature of 25,000 K, flagging anything with WD parameters outside of these ranges and removing them from further analysis. Of the 74 systems for which this calculation was possible, 12 have WD effective temperature outside of the acceptable range, and 2 have WD mass outside of the acceptable range. With 1 overlapping system, a total of 61 WD+MD systems have acceptable WD mass and effective temperature values for further analysis. Of these, 56 are not experiencing Roche overflow with $> 95\%$ confidence.

I assumed two different M dwarf mass-loss rates for different samples in my target selection. The two rates are 1×10^{-14} $M_{\odot}$/yr, which is the median of the values reported in Wood et al. (2021), and 6×10^{-13} $M_{\odot}$/yr, which is the highest of the values reported in Wood et al. (2021). For each of these two cases, I calculate the expected calcium abundance and compare to two detectability thresholds: log N(Ca)/N(H) = -8, (a conservative cut), and log N(Ca)/N(H) = -9.284, (the lowest Ca abundance measured for a WD+MD in Zuckerman et al. (2003)).

In addition to the 95% confidence condition for the system to not be experiencing Roche overflow, I assess the confidence of expecting detectable calcium using three combinations: the median 0.5 $\dot{M}_{\odot}$ M dwarf wind rate with the conservative log N(Ca)/N(H) = -8 detectability threshold, the median wind rate with the more generous log N(Ca)/N(H) = -9.284 detectability threshold, and the high 30 $\dot{M}_{\odot}$ M dwarf wind rate with the more generous detectability threshold.

I allowed each parameter in the relevant calculations to vary within a Gaussian distribution centered on the reported value, and with standard deviation equal to the reported uncertainty, except for the M dwarf assumed wind rates and the calcium detectability thresholds. For each system, I recalculated the expected calcium abundance and the Roche radius 50,000 times using system parameters resampled independently from Gaussian distributions using numpy.random.normal(). Note that while the calcium detectability thresholds are constant, the M dwarf radius is also allowed to vary within its Gaussian distribution, and recalculated 50,000 times for comparison against the Roche radius. Only those systems for which both conditions are met at least 95% of the time make it to the relevant sample.

2.2.1 The Samples

I defined 5 samples of promising targets from the original 90 binary systems in the SDSS WDMS binary catalogue (Rebassa-Mansergas et al., 2012). All five samples require that the system not be experiencing Roche overflow with $> 95\%$ confidence. Four of the samples also require that the WD mass be below 1.1 $M_{\odot}$ with the exception being the "Visible Ca" sample. There are three different temperature constraints, which are physically motivated, and described in more detail below. The "Platinum", "Gold", and "Silver 1" samples differ in their assumed M dwarf wind rate, calcium detectability threshold, and maximum allowed WD effective temperature and mass are summarized in table 2.1.

Table 2.1: The selection criteria for the five samples used in this thesis. The 'Sample' column refers to the sample name. The 'Total' column refers to the total number of systems that meet all the criteria for the relevant sample. The 'Wind Dominated?' column refers to whether a check was made to ensure the systems are not experiencing Roche lobe overflow. 'Assumed $\dot{M}$' is the wind mass-loss rate that is assumed when calculating an expected calcium abundance and 'Min Ca/H' is the calcium detectability threshold (see section 2.2). The 'WD T_{eff}' and 'WD Mass' columns refer to the maximum allowed WD effective temperature and WD mass.

Criteria for the Different Samples						
Sample	Total	Wind Dominated?	Assumed $\dot{M}$ ($M_\odot$ / yr)	Min. Ca/H (log N(Ca)/N(H))	WD T_{eff} (K)	WD Mass ($M_\odot$)
Platinum	28	yes	1×10^{-14}	-8	$< 20,000$	< 1.1
Gold	46	yes	1×10^{-14}	-9.284	$< 20,000$	< 1.1
Silver 1	56	yes	6×10^{-13}	-9.284	$< 25,000$	< 1.1
Silver 2	8	yes	-	-	$< 10,000$	< 1.1
Visible Ca	2	yes	-	-	$< 20,000$	-

Platinum Sample

This sub-sample contains 28 systems, and is subject to the most stringent of the constraints for calcium detectability. I take the median M dwarf wind mass-loss rate from Wood et al. (2021) of 1×10^{-14} $M_\odot$/yr, and use a calcium detectability threshold of Ca/H> -8, as 7 of the 9 WD+MD pairs in Zuckerman et al. (2003) with Ca/H measurements or upper limits lie below this threshold. Additionally, the white dwarf mass and temperature must be within a range for which the timescale for metals to settle out of the atmosphere is well understood. Based on the diffusion timescale tables for DA WDs from Bauer & Bildsten (2019) covering 0.38, 0.6, and 0.9 $M_\odot$ WDs, and the typical mass range of carbon/oxygen core WDs being $0.45 - 1.05$ $M_\odot$ Hansen (2004), I selected an upper limit of 1.1 $M_\odot$ for our WD masses. My temperature limit of $20,000$ K was motivated by the $20,000$ K limit mentioned in

Zuckerman et al. (2003) stated to be the temperature below which heavy elements have short diffusion timescales and negligible radiative levitation (Chayer et al., 1995) and the 20,500 K limit of the Bauer & Bildsten (2019) models. Although 25,000 K is sometimes used as the limit where radiative levitation becomes important, I wanted to be conservative with the WD temperature constraints on this sample. Six targets that would have otherwise met the Platinum sample criteria had WD effective temperatures between 20,000 K and 20,500 K. These targets were instead assigned to the Silver 1 sample. Lastly, the binary pair must have a wide enough separation to be in the wind-dominated regime (no Roche overflow), and the binary pair must have a separation close enough for the expected flux of wind material at the white dwarf's location to produce detectable metal lines using the aforementioned M dwarf wind mass-loss rate and calcium detectability threshold.

Gold Sample

This sub-sample contains 18 systems in addition to the 28 systems in the platinum sample. I take the median M dwarf wind mass-loss rate from Wood et al. (2021) of $1{\times}10^{-14}$ $M_{\odot}$/yr, and relax the calcium detectability threshold to Ca/H> -9.284, the lowest calcium abundance reported for a WD+MD pairs in Zuckerman et al. (2003), excluding upper limits. As with the platinum sample, an upper limit of 1.1 $M_{\odot}$ was used for our WD masses, and a temperature limit of 20,000 K was used for our WD effective temperatures. Two targets that would have otherwise met the Gold sample criteria had WD effective temperatures between 20,000 K and 20,500 K. These targets were instead assigned to the Silver 1 sample. The same restrictions regarding pair separation apply here, but for the more optimistic calcium detectability

threshold Ca/H> −9.284.

Silver 1 Sample

This sub-sample contains 10 systems in addition to the 46 systems in the gold and platinum samples. I take the highest M dwarf wind mass-loss rate from Wood et al. (2021) of 6×10^{-13} $M_{\odot}$/yr, and use a calcium detectability threshold of Ca/H> −9.284, the lowest calcium abundance reported for a WD+MS pairs in Zuckerman et al. (2003), excluding upper limits. As with the platinum and gold samples, an upper limit of 1.1 $M_{\odot}$ was used for our WD masses, however, a temperature limit of 25,000 K was used for our WD effective temperatures. Works such as Koester (2009) use 25,000 K as the temperature limit below which heavy elements should diffuse through the atmosphere due to gravity. Above 25,000 K, I cannot be confident that any detected heavy elements such as calcium are due to continuous accretion (Schatzman, 1945), but I did not want to entirely exclude systems with WD effective temperatures between 20,000 K and 25,000 K. The same restrictions from the gold sample regarding pair separation apply here, but using the higher M dwarf wind mass-loss rate of $6{\times}10^{-13}$ $M_{\odot}$/yr.

Silver 2 Sample (Cool WD Sample)

This sub-sample contains 8 systems. I do not check for calcium detectability in this sample, so no M dwarf wind mass-loss rate or calcium detectability threshold needed to be assumed. As with the previous samples, an upper limit of 1.1 $M_{\odot}$ was used for our WD masses, however, a temperature limit of 10,000 K was used for our WD effective temperatures. The point of this sample was to isolate the pairs with

the coldest WDs, since for a given abundance, the corresponding equivalent width will be much larger in a colder WD than a hotter one (Zuckerman et al., 2003). The separation of these binaries must still be large enough that the system is not experiencing Roche lobe overflow.

Visible Ca Sample

This sample was defined by looking at interactive SDSS spectra for 89 of the 90 targets through the Montreal White Dwarf Database (SDSS J233928.35-002040.0 did not have an SDSS spectrum available on the Montreal White Dwarf Database). I identified 8 systems that showed a visible signature of of Ca II K absorption. Of these 8 systems, two were too hot (SDSS J211428.41-010357.2 and SDSS J085746.18+034255.3), and one was overfilling its Roche lobe (SDSS J223530.61+142855.0). All of the remaining 5 systems show spectra that are white dwarf dominated, and are shown in figure 2.3. The least WD dominated system, SDSS J121010.13+334722.9, has a $\sim$ 9% M dwarf contribution at Ca II H&K wavelengths, compared to $\sim$ 1% for the other systems. SDSS J121010.13+334722.9 also does not show Balmer absorption and does not have a listed WD effective temperature in the SDSS WDMS binary catalogue or in Morgan et al. (2012). I remove it from further analysis, but note that Pyrzas et al. (2012) has done a full analysis on this system. SDSS J015225.38-005808.5 and SDSS J184412.58+412029.4 had Ca II H&K absorption features that could be fit with polluted WD models (Simon Blouin, private communication), whereas SDSS J213218.11+003158.8 and SDSS J164615.60+422349.2 had weaker absorption features and were considered not viable to fit with the Blouin models (Simon Blouin, private communication). SDSS J213218.11+003158.8 and SDSS J164615.60+422349.2

are part of the platinum sample, but will not be considered further in the visible sample. Thus, there are only two targets in the visible Ca sample, SDSS J015225.38-005808.5 and SDSS J184412.58+412029.4.

2.2.2 Measuring Calcium Equivalent Width in a WD+MD Combined Spectrum

M dwarfs can remain magnetically active for billions of years after forming (West et al., 2008). Additionally, M dwarfs in close binary pairs with WDs remain magnetically active for longer than field M dwarfs, potentially due to tidal effects and angular momentum exchange with the WD (Morgan et al., 2012). Stellar chromospheric calcium emission at the Ca II H&K lines are a common activity indicator for M dwarfs (Marvin et al., 2023). These emission lines, vacuum wavelengths 3933.663 (K line) and 3968.469 (H line) Å (Johnson et al., 2022), are occurring at the same wavelengths as the expected Ca absorption features from the WD.

All the SDSS spectra from the SDSS WDMS binary catalogue (Rebassa-Mansergas et al., 2012) have a WD component and an M dwarf component. They are unresolved binaries, and the spectra of the WD and M dwarf components cannot be obtained individually because they are too close together on the sky for the stellar components to be spatially resolved by SDSS. Though the continuum of the WD tends to dominate at blue wavelengths ($\sim 3800-5000$ Å) for most of the spectra, ~ 40 of the 90 systems show calcium emission lines. These emission lines are dominating over any potential WD absorption that may be present. I believe the source of this emission is magnetic chromospheric emission from the unresolved M dwarf companion. There is clear Hα emission in many of the target spectra, indicating a magnetically active M dwarf

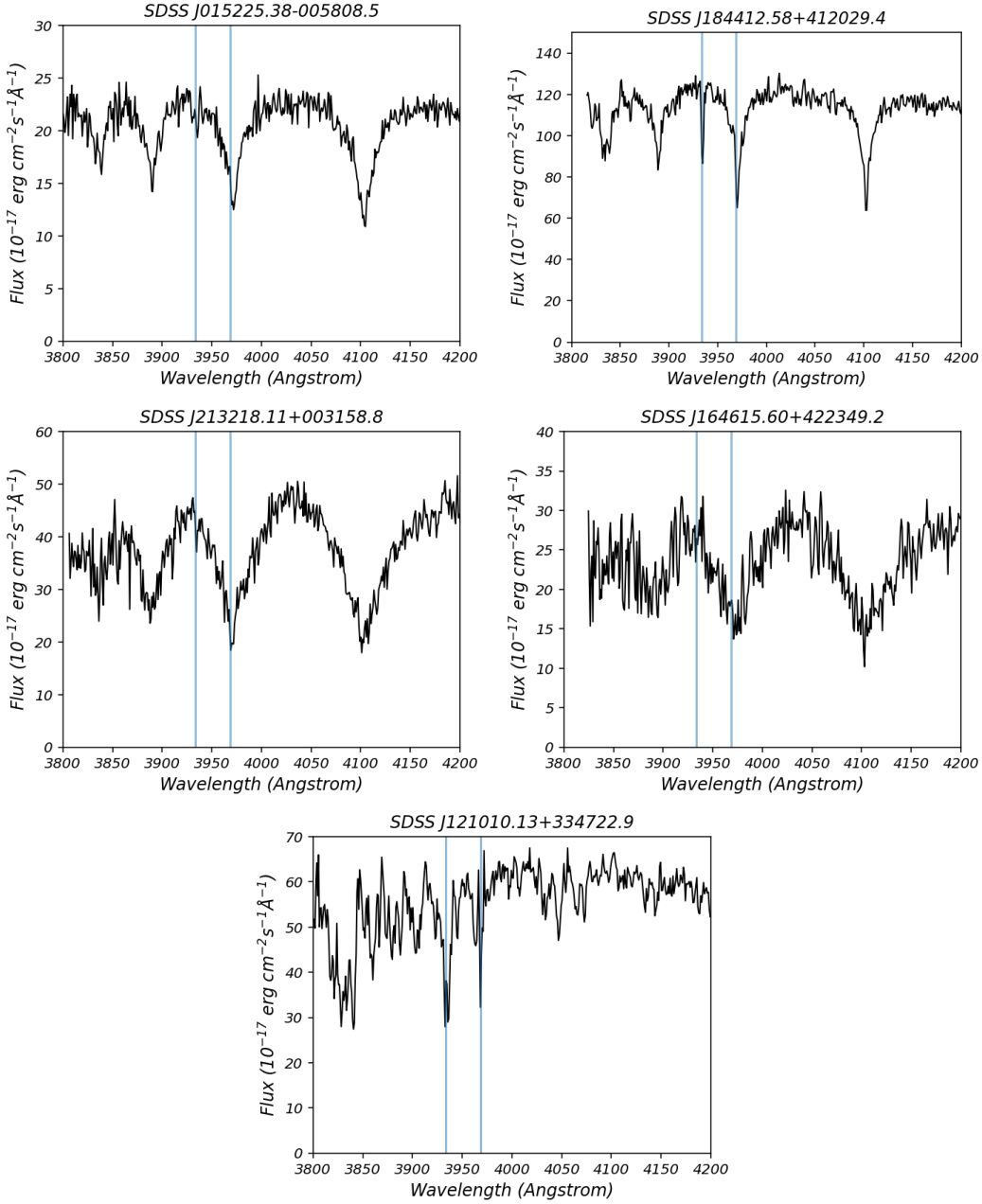

Figure 2.3: Spectra of the five systems that show visible calcium absorption and are neither too hot nor in the regime of Roche lobe overflow. The spectra are cropped to show the Ca II H&K line region. The blue vertical bars show the vacuum wavelength for the Ca II H&K lines, with Ca II K being the shorter-wavelength feature. Recall that the Ca II H line overlaps with the broad Hϵ Balmer absorption feature, though SDSS J121010.13+334722.9 does not show Balmer absorption.

companion in those systems. Since calcium is also a magnetically sensitive element, it seems reasonable to assume the calcium emission lines are from the M dwarf in targets that also display Hα emission. Additionally, for another ~ 40 systems, neither emission nor absorption is apparent at the Ca II H&K wavelengths. I determined that there should be detectable WD Ca II H&K absorption features in $\sim 30-50$ of these PCEB systems, just among those not experiencing Roche overflow, but my visible calcium sample only contains two viable targets. I believe that calcium emission lines from magnetically active M dwarfs are being combined with the calcium absorption features and netting out to an overall emission or inconclusive signal. Due to the moderate resolution of SDSS (R$\sim$1800 near the Ca H&K lines), the potential WD absorption signals cannot be disentangled from the M dwarf emission lines, as calcium absorption features in DAs are much narrower ($\lesssim$ 1 Å) than their broad Balmer absorption features (Zuckerman et al., 2003). If all M dwarfs in PCEB systems are magnetically active, as suggested by Rebassa-Mansergas et al. (2013), then this is an issue that should affect most attempted M dwarf wind mass-loss rate measurements using PCEB systems. Developing and implementing the methodology to disentangle M dwarf calcium emission from potential WD calcium absorption is one of the main results of this thesis.

To determine how much, if any WD calcium absorption there is in these spectra, I need to separate the WD and M dwarf components. This is difficult, because publicly available WD stellar atmosphere models used to make model spectra do not include metal lines, so non-polluted models must be used. Additionally, the opacity sources in M dwarf atmospheres are not completely understood, so M dwarf spectral templates compiled using real spectra must be used instead of models.

Equivalent width is the width in wavelength units that a line (either absorption or emission) would have such that when multiplied by the continuum level the area of the rectangle is the same as the area of the spectral line. WD properties affect how the equivalent width of a pollutant will appear with respect to its abundance. In general, the equivalent width created by a set abundance decreases for hotter objects, such that the abundance needed to create a detectable line is much higher for hotter objects (Zuckerman et al., 2003). Surface gravity also affects the absorption lines of pollutants, especially above $T_{eff} = 12,000$K, with higher surface gravities producing wider lines (Chandra et al., 2020).

Rauscher & Marcy (2006) suggest a correlation between the equivalent widths of Ca II H&K emission lines, and Hα emission lines. This correlation is suggested to hold true above some threshold where the different layers of the chromosphere in which these lines form become coupled (Rauscher & Marcy, 2006; Marvin et al., 2023). This suggests that if I can isolate the M dwarf contribution in the region of the Hα line (vacuum wavelength $\sim$6564.5 Å), I can correlate the M dwarf Hα emission equivalent width to an expected M dwarf Ca K emission equivalent width.

M Dwarf Hα Emission

Luckily, non-polluted WD models work really well for removing the WD contribution in the region around the Hα Balmer line, where I am interested in removing the WD continuum and Balmer absorption contributions only. The WD effective temperatures and surface gravities were found in Rebassa-Mansergas et al. (2016) based on the best fit using the Koester (2010) model grid in their spectral decomposition and fitting routine. Therefore, I use the WD effective temperatures and

surface gravities and their uncertainties from the SDSS WDMS binary catalogue to determine the WD flux contribution in the region around the Hα Balmer line. The Koester (2010) model grid covers WD surface gravities from log g = 6.5 to 9.5 dex (where g is in cm/s^2) in increments of 0.25 dex, and WD effective temperatures from T_{eff} = 5000 K to 20,000 K in steps of 250 K, from 20,000 K to 30,000 K in steps of 1000 K, and also includes T_{eff} = 32,000, 34,000, 35,000, 36,000, 38,000, 40,000, 45,000, 50,000, 60,000, 70,000, and 80,000 K. For each system that appears in at least one of my 5 samples, I first interpolate the entire grid of Koester WD models to the wavelength grid of the WD+MD target's SDSS spectrum. This is done using interp1d from scipy.interpolate to linearly interpolate the WD model flux values from the WD model wavelength grid onto the WD+MD wavelength grid. Then, then entire grid of models (hereafter 'interp_models') is passed to RegularGridInterpolator from scipy.interpolate. RegularGridInterpolator uses 'points' to define the regular grid in n dimensions. I apply 'points' to define three dimensions, Koester WD effective temperatures, Koester WD surface gravities, and the interpolated WD+MD wavelength grid. For every combination of Koester WD effective temperature, Koester WD surface gravity, and interpolated WD+MD wavelength, there is a single Koester WD flux value contained in 'interp_models'.

Next, the interpolation to match the WD effective temperature and surface gravity from the WD+MD target begins. The WD surface gravity and effective temperature are passed from the reported SDSS WDMS binary catalogue values. RegularGridInterpolator is called to retrieve the flux value associated with each WD+MD wavelength for the effective temperature and surface gravity combination. These are the

unscaled interpolated flux values for the Koester model match to the WD+MD system. While a scale factor is theoretically able to be determined from the WD radius and distance, I encountered an issue with reported distances in that gave poor scale factors to many of the systems. To scale the model fluxes, I use scipy.optimize.curve_fit to determine a scale factor for the interpolated flux values. I chose the scale factor that provides the best match between the scaled interpolated flux values and the WD+MD SDSS flux values on the wavelength range from 3800 to 4300 Å. This wavelength range was chosen because it covers the most WD dominated region of the spectra that is not subject to the flux calibration issues of SDSS spectra near the blue end of the spectra (Rebassa-Mansergas et al., 2007).

To estimate the uncertainty on these interpolated flux values, uncertainties on the WD surface gravity and effective temperature values are passed through the interpolation described in the above paragraph as an array of 1000 values generated from numpy.random.normal(). Specifically, the first 1000 values from the resampled values previously generated for determining the Roche overflow and calcium detectability confidence. For a few systems, the surface gravity or temperature resamples fell outside of the coverage of the Koester model grid. When this occurred, the previous value was repeated. For example, if the resampled effective temperature was too low in run 3, the run 2 effective temperature and the run 3 surface gravity would be used. The standard deviation of flux at each wavelength was taken using numpy.std(), and the list of scaled fluxes and uncertainties were saved for each system. An example best-fit Koester model and 1000 resamples is shown in figure 2.2.

With this, I was able to isolate the M dwarf flux contribution in the region around Hα for all my targets. I subtracted the best-fit scaled Koester models from each SDSS

WD+MD spectrum, and the SDSS spectrum flux uncertainties were added in quadrature to the Koester model uncertainties to determine the total flux uncertainty at each wavelength for the 'M dwarf isolated' (also called 'WD subtracted') spectrum. Since SDSS flux uncertainty values are given as inverse variance, I first converted these to standard deviation form before adding them to the Koester model flux uncertainties. The Hα region in the WD subtracted spectrum is fit by a two-component model: a degree 2 polynomial for the local continuum and a Voigt function for the Hα emission line from 6450 to 6700 Å. This 7 parameter model fit is shown in figure 2.4. This model is defined over a wavelength grid centered on 6575 Å with a 250 Å spread. The shifted grid is renormalized such that the shifted wavelength coverage is $\sim (-1, 1)$. Performing the model fit on this shifted wavelength grid helps keep the model parameter values small, reducing the risk of numerical precision issues.

For the emission line model, I used astropy.modeling.models.Voigt1D, a one-dimensional Voigt profile model that is parameterized by the position of the emission peak, the amplitude of the Lorentzian component, the full-width-half-maximum (FWHM_L) of the Lorentzian component, and full-width-half-maximum (FWHM_G) of the Gaussian component as parameters, along with optional bounds for each parameter. The initial guess for the peak location is the vacuum wavelength for Hα (6564.5 Å). The initial guess for the amplitude is the difference between the maximum and minimum flux values between 6500 and 6650 Å. Both full-width-half-maximum (FWHM) initial guesses are set to 2 Å. I set bounds on each of the four parameters, with the peak location being allowed to vary up to 10 Å in either direction

(6554.5 to 6574.5 Å, (-10/175) to (10/175) shifted values). The Lorentzian amplitude is allowed to vary from 0 to 1.5 times the initial guess. Each FWHM is allowed to vary from 10^{-12} to 15 ((15/175) shifted values). 10^{-12} is used instead of 0 because FWHM values of 0 are unphysical, and cause inflated uncertainties on the model amplitude. Since the amplitude is allowed to be 0, the model is already able to account for the case of no emission line. For the continuum model, I used astropy.modeling.polynomial.Polynomial1D, a one-dimensional polynomial model. I specify a second degree polynomial which is of the form $c_0 + c_1 x + c_2 x^2$, and do not impose any initial guesses or bounds on these parameters. Thus, my two-component model is simply the sum of the Voigt1D and Polynomial1D components described above.

Next I define a Spectrum1D object which contains the flux values of the WD subtracted (M dwarf isolated) WD+MD SDSS spectrum, the shifted wavelength values, and the total flux uncertainty specified to be standard deviation using astropy.nddata.StdDevUncertainty. Then, I use specutils.fitting.fit_lines to find the best fit parameters for my Spectrum1D object, given the model described above. I specify a window from -1 to 1 on the shifted wavelength grid, a maximum iteration of 10,000, tell fit_lines that the uncertainties on Spectrum1D are standard deviations (weights='unc'), and set get_fit_info=True so I can recover the uncertainties associated with the individual parameters. The individual parameter uncertainties are recovered by taking the square root of the diagonalized parameter covariance matrix. I use version 1.19 of specutils. Note that the Spectrum1D object has been updated to the Spectrum object starting in version 2.0 (released June 2025), and Spectrum1D will be deprecated in version 2.1.

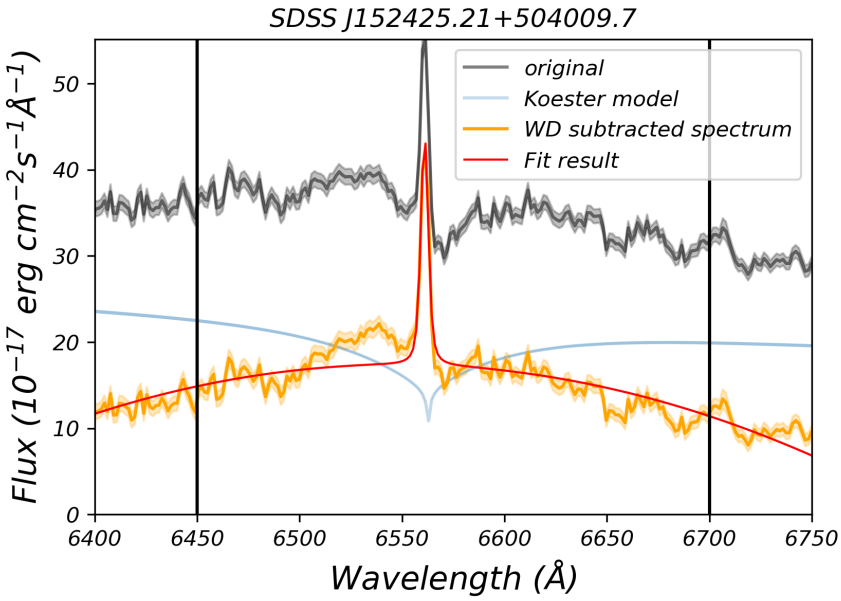

Figure 2.4: Our 7 parameter fit on the M dwarf isolated (WD subtracted) SDSS spectrum in the Hα region. The original WD+MD spectrum and flux uncertainty is shown in dark grey. The best fit Koester model is shown in blue. The WD subtracted spectrum and flux uncertainty is shown in orange, where the flux uncertainty is the combined uncertainty of the original spectrum and of the Koester model. The model fit is shown in red. Black vertical bars show the region over which the model is fit to the WD subtracted spectrum.

The problem with using the individual parameter uncertainties to determine the overall model uncertainty is that some of the model parameters are correlated. For example, the individual uncertainties on the FWHM Gaussian and Lorentzian components may be high because the data is fit well both by a large FWHM_L plus small FWHM_G, and a small FWHM_L plus large FWHM_G. It would overestimate the total model uncertainty to let these two values vary independently within their individual uncertainties, since the data is never fit well by a large FWHM_L plus large FWHM_G, or a small FWHM_L plus small FWHM_G. For this reason, I opted to use a Markov Chain Monte Carlo (MCMC) to sample the distribution of parameters for each system in a way that accounted for the dependencies of certain model parameters. MCMC techniques generate random numbers in a dependent fashion, where the numbers are generated sequentially and each depends on its predecessors. Because of correlations when generating the sequential chain, it is useful to thin the chain by keeping only every n^{th} entry. There is a period in which the sampled parameters depend on the initial conditions (called the 'burn-in'), after which the chain ceases to show systematic trends (Wall & Jenkins, 2012). To implement the MCMC, I used emcee.EnsembleSampler (Foreman-Mackey et al., 2013), an ensemble MCMC sampler that allows multiple chains to be generated simultaneously and independently. I used emcee.EnsembleSampler with a flat prior based on the original Voigt parameter constraints. Using step sizes of 10^{-4} for each parameter and 32 random walkers (which explore the parameter space in random directions through sucessive steps), I run the MCMC for a chain length of 10,000. I discard the first 2000 steps from each chain to account for burn-in, take only every 15 steps from the chain using 'thin=15' to account for correlations when generating the chain, and flatten the chain across

the ensemble. This leaves us with the best fit distribution for each of the 7 model parameters.

The emcee results are saved for each system, and passed to a function I wrote to determine the Hα equivalent width and associated uncertainty. The equivalent width is calculated using scipy.integrate.quad() on fits for the M dwarf Hα local continuum and emission line Voigt profile, obtained using samples from the joint posterior of the model parameters. The standard equation for equivalent width is

$$EW = \int_{\lambda_1}^{\lambda_2} \frac{F_{cont.} - F_{total}}{F_{cont.}} d\lambda, \tag{2.2.9}$$

where $F_{cont.}$ is the flux of the continuum, and F_{total} is the total flux of the spectrum, continuum plus spectral lines. The integral to calculate the equivalent width is taken over the wavelength range covered by the spectral line of interest, but taking the integral over a wider wavelength range should not significantly impact the result unless other spectral lines are present.

For the M dwarf Hα emission line, we have:

$$EW = \left(\int_{6450}^{6700} \frac{F_{MD_{cont.}} - (F_{MD_{cont.}} + F_{MD_{H\alpha}})}{F_{MD_{cont.}}} d\lambda \right) \text{Å} \tag{2.2.10}$$

I calculate the equivalent width for each set of model parameters from the emcee results of each system, to obtain the Hα EW and uncertainty for each of my targets. Since my model was defined on the shifted wavelength range, we need to multiply the resultant EWs by 175 to bring them back to proper Angstrom units. I take the best-fit Hα EW to be the median of the EW values, and the EW uncertainty to be the standard deviation of the EW values. The M dwarf Hα EWs and uncertainties

are presented as a function of M dwarf mass in figure 2.5.

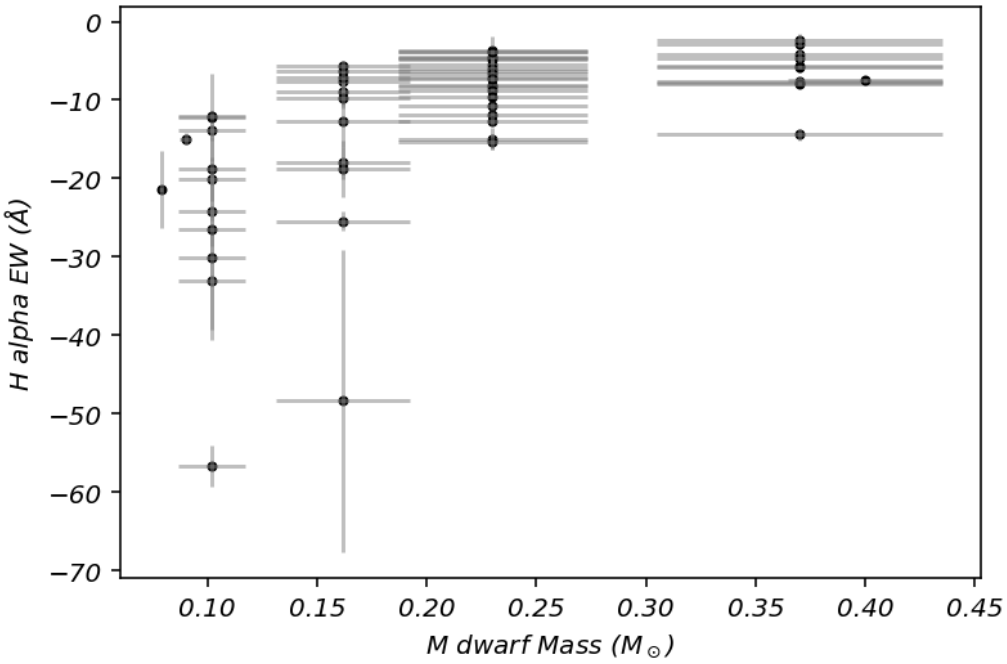

Figure 2.5: Calculated Hα EW and uncertainties for each system compared to the M dwarf mass and mass uncertainty. Uncertainties in mass are lower for lower mass systems because the difference in mass between spectral types is smaller for lower mass M dwarfs as defined by "A Modern Mean Dwarf Stellar Color and Effective Temperature Sequence" (Pecaut & Mamajek, 2013), which we used to determine the M dwarf masses.

In figure 2.5, it is apparent that the lower mass stars tend to have larger (more negative) Hα emission EWs than the higher mass stars in this sample. Works such as West et al. (2008) and West et al. (2011) have identified a trend of increasing fraction of active stars with decreasing mass, with Hα emission activity in $< 5\%$ of the population for the most massive M dwarfs (spectral type M0) and $> 75\%$ of the population for the least massive M dwarfs (spectral type M9). West et al. (2011) also show that lower mass M dwarfs stay magnetically active for longer. Regarding the observed trend of more negative Hα emission EW for lower mass M dwarfs, Hawley

et al. (1996) note that lower mass M dwarfs have lower continuum flux, making it easier to detect weaker lines in lower mass stars. They state that an emission feature with an Hα EW of -1 Å in an M5 star corresponds to less total flux in the Hα line than an emission feature with an Hα EW of -1 Å in an M0 star. This suggests that for two M dwarfs of equal magnetic activity, the lower mass M dwarf will show a more negative Hα EW than the higher mass M dwarf. Indeed, Reid et al. (1995) report the mean of the ratio of Hα luminosity to bolometric luminosity remained roughly constant for spectral types M0-M6, indicating constant average activity for M dwarfs in their sample (stars from the Hyades cluster).

M Dwarf Hα - Ca K Emission Correlation

Once I had isolated the M dwarf contribution in the region of the Hα line, I wanted to correlate the M dwarf Hα emission equivalent widths to expected M dwarf Ca K emission equivalent widths based on the relation suggested by Rauscher & Marcy (2006). Instead of directly using the correlation from Rauscher & Marcy (2006), I decided to define my own using a sample of magnetically active M dwarf stars from West et al. (2011). This choice was motivated by the Rauscher & Marcy (2006) correlation only containing 8 points above their reported 3 Å calcium EW threshold, the threshold above which they expect a correlation in Hα and calcium EWs. Additionally, it is the Ca II H EWs that are shown on their correlation. The Ca II H line also overlaps with the WD Hϵ Balmer absorption line (3970 Å), so the Ca II K line is more useful for my analysis because it does not suffer from as extreme contamination.

The West et al. (2011) sample of M dwarfs contained over $70,000$ stars. By selecting only those that were confirmed single stars, with Hα EWs above an activity

threshold of 0.75 Å, and Ca II K EWs above an activity threshold of 1.5 Å, relative uncertainties on both EW measurements below 25%, and manually removing a few systems with bad spectra (ie. large chunks of missing flux measurements in the Ca II K region), I was left with 192 stars. As the West et al. (2011) sample did not provide masses for the M dwarfs, I opted to divide the sample into partially and fully convective systems based on spectral type. The transition between fully and partially convective M dwarfs occurs between spectral types M3 and M4, and West et al. (2011) provides only full integer spectral types. I assigned spectral types M0-M3 to the partially convective sample and spectral types M4-M9 to the fully convective sample. The resultant subsamples both had 96 stars.

Next, I wanted to test whether these two samples were consistent with being drawn from the same distribution. I used the one-dimensional two-sample Kolmogorov-Smirnov (K-S) test, and the two-dimensional two-sample K-S test with the standard significance of 0.05. In addition to the samples with relative EW uncertainties below 25%, I defined three more sets of fully and partially convective M dwarf samples to see if the results changed based on which EW uncertainty constraints are chosen. These sets all had the same activity threshold cuts, and confirmed single star constraints. For the second set, I required the absolute EW uncertainties to be below 1 Å with no constraint on the relative uncertainties. For the third set, I required absolute EW uncertainties below 1 Å and relative EW uncertainties below 25%. For the last set, I required that either the absolute EW uncertainties were below 1 Å or the relative EW uncertainties were below 25%. The four sets are shown in figure 2.6 along with the total number of fully and partially convective M dwarfs that meet the criteria.

For the one-dimensional two-sample K-S tests, I rejected the null hypothesis that

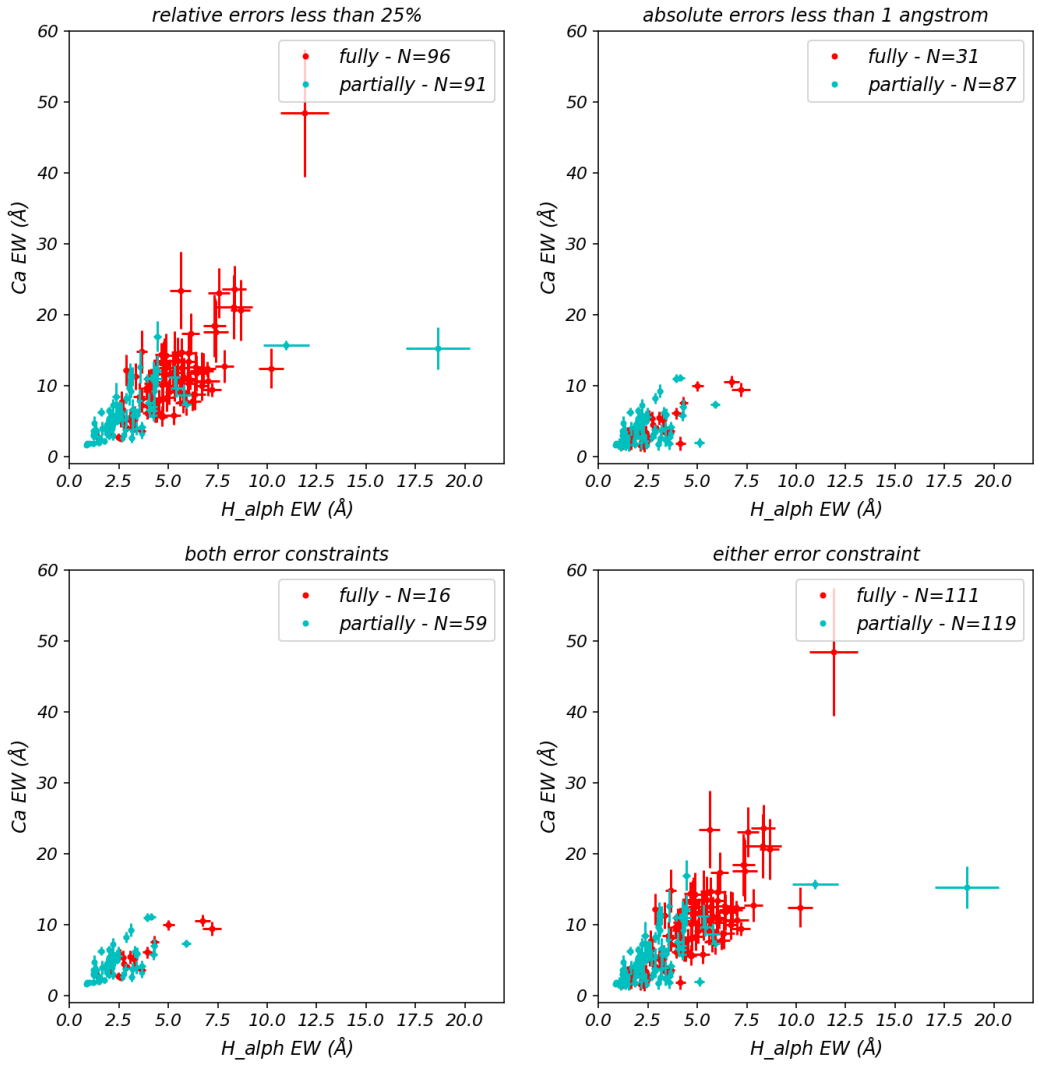

Figure 2.6: Four samples showing the correlation between Ca II K EW and Hα EW in magnetically active M dwarfs under four different EW uncertainty constraints: EW relative uncertainties below 25% of the EW value, absolute EW uncertainties less than 1 Å, both EW absolute uncertainties less than 1 Å and EW relative uncertainties below 25% of the EW value, and either EW absolute uncertainties less than 1 Å or EW relative uncertainties below 25% of the EW value. Partially convective systems are shown in cyan and fully convective systems are shown in red.

the Hα EWs in the partially convective and fully convective M dwarf samples were drawn from the same distribution with $> 99\%$ confidence for all four sets. I also rejected the null hypothesis that the Ca II K EWs in the partially convective and fully convective M dwarf samples were drawn from the same distribution with $> 99\%$ confidence for the 25% uncertainty constraint set and the $< 25\%$ or 1 Å uncertainty constraint set, but I was not able to reject the null hypothesis for the 1 Å uncertainty constraint set or the 1 Å and $< 25\%$ uncertainty constraint set. For the two-dimensional two-sample K-S tests, I rejected the null hypothesis that the EW correlations in the partially convective and fully convective M dwarf samples were drawn from the same distribution with $> 99\%$ confidence for all four sets. Based on these results, I decided to define separate Hα - Ca K EW correlations for the fully convective and partially convective M dwarfs.

Of the four sets of uncertainty constraints described above, I opted to use the requirement for absolute EW uncertainties below 1 Å and relative EW uncertainties below 25%. Although this results in the smallest number of systems contributing to the correlation, it is more robust than the absolute EW uncertainties below 1 Å constraint, while not being biased towards systems with large EWs like the relative EW uncertainties below 25% constraint. I defined log-linear correlation functions ($y = x^m \times 10^b$, where x is the Hα EWs and y is the Ca II K EWs) and found the best fit using scipy.optimize.curve_fit on bootstrapped Hα and Ca II K EW values resampled within Gaussian distributions defined by their reported values and uncertainties (n=1000). Initial guesses of $m = 0.8$ and $b = 0$ were used. For the partially convective sample the median of the resultant parameters were $m = 0.67$ and $b = 0.41$. For the fully convective sample the median of the resultant parameters were $m = 0.90$ and $b = 0.26$.

From the 1000 best fit parameters, the standard deviations in Ca II K EWs were calculated as a function of Hα. The resultant correlations and associated uncertainties are shown in figure 2.7.

For each of my M dwarf isolated (WD subtracted) targets, the Ca II K EW comes from the M dwarf Hα EW value applied to the best fit correlation function. The target M dwarf's spectral type determines which correlation function will be used. Following the division used to separate the West M dwarfs, spectral types M0-M3 are assigned partially convective and spectral types M4-M9 are assigned fully convective. None of my target WD+MD systems had spectral types between M3 and M4. The only one of my target systems that did not contain a whole-integer M dwarf was SDSS J102857.78+093129.8, which contains an M2.5 secondary.

To get the Ca II K EW uncertainty, the Hα EW is resampled as a Gaussian distribution and applied to the best fit correlation function. The Ca II K EW uncertainty due to uncertainty in Hα EW is added in quadrature to the Ca II K EW uncertainty due to the uncertainty in the correlation at the median Hα EW. The target M dwarf Ca II K and Hα EWs and uncertainties are shown in figure 2.8 for systems with Hα EW below 20 Å.

Total Ca II K Equivalent Width

The next piece we need is the total Ca II K EWs of the WD+MD spectra. For each of my targets, I fit the local continuum of the WD+MD with a degree 2 polynomial using Polynomial1D. The procedure here is similar to fitting the M dwarf Hα emission line, but without the added complexity of simultaneously modeling the Voigt emission. An example spectrum fit is shown in figure 2.9. As before, I define a wavelength grid,

this time centered on 3930 Å and covering a spread of 40 Å. The wavelength grid is normalized (divided by 20) such that the wavelength range considered by the model is from -1 to 1. The flux uncertainties from SDSS are converted from inverse variance to standard deviation. Then the region around the Ca II K vacuum wavelength is masked out (3030 to 3940 Å), so that it does not impact the local continuum fit. The same window is used regardless of if there is visible Ca II K emission, for consistency. As before, fit_lines is used to determine the best fit model parameters and their associated uncertainties. Because I am not modeling a Voigt component here, I trust the individual parameter uncertainties are sufficiently independent that determining the model uncertainty using emcee is not necessary here. 1000 resamples of the continuum fit, allowing each parameter to vary in a Gaussian distribution defined by its best fit value and uncertainty, are used when calculating the Ca II K EW. For each of the resampled continua, an integrand is defined over the region where Ca II K is expected (this is the same as the masked region). Then, the integration is performed on the integrand on the original wavelength range using scipy.integrate.simpson(). The EW is the median of the resampled integrals, with uncertainty equal to the standard deviation of the resampled integrals.

White Dwarf Ca K Absorption

Now that I have the Ca II K EWs for the total WD+MD spectra and the CA II K EWs for the MD contribution of each system, I am able to recover the WD Ca II K contribution for each system. For a spectrum with two sources, the net EW of a spectral line is the sum of the EWs of that spectral line from each of the contributing

sources, weighted by their continuum levels:

$$EW_{total} = \frac{EW_1 \times F_{cont._1} + EW_2 \times F_{cont._2}}{F_{cont._{total}}}, \tag{2.2.11}$$

where

$$F_{cont._{total}} = F_{cont._1} + F_{cont._2} \tag{2.2.12}$$

I obtain $F_{cont._{total}}$, the Ca II K region local continuum of the WD+MD spectrum, by taking the median flux value of the total WD+MD continuum between 3910 and 3930 Å. The total continuum uncertainty is taken to be the standard deviation of the flux values between 3910 and 3930 Å, as the difference in flux over this range dominates over the individual flux uncertainties.

To obtain the M dwarf Ca II K region local continuum, I compile magnetically active M dwarf templates from West et al. (2011) based on spectral type. There are 192 of these magnetically active M dwarfs that are confirmed to be single stars and have appropriate Ca II H&K EWs and EW uncertainties. Three systems with spectral type 3 were removed due to issues with NAN values in their spectra. The number of West et al. (2011) targets used to create each spectral type template are detailed in table 2.2. For each of my targets, the West et al. (2011) template that matched the spectral type of the M dwarf was normalized to match with the M dwarf isolated spectrum over the wavelength range $8300 - 8400$ Å. This wavelength range was chosen because it is the most M dwarf dominated region that has a flat local continuum. The M dwarf Ca II K region local continuum is taken to be the median of the fitted West et al. (2011) template between 3910 and 3930 Å. The median of the template flux uncertainties (taken as the median average deviation in flux between

Table 2.2: This table shows how many magnetically active M dwarf spectra from West et al. (2011) were used to make the templates for each spectral type, and how many of my target WD+MD systems contained an M dwarf of that spectral type. There were no West Spectra available for spectral types 8 and 9, so the 7 spectra for spectral type 6 and the 2 spectra for spectral type 7 were combined into the 6+ category. Of my targets, there was one spectral type 9 and one spectral type 7 star, the rest were type 6 or earlier. Of all the target stars, all of them are whole-integer spectral types except for system SDSS J102857.78+093129.8, which has spectral type 2.5. The West spectral type 3 template was a better fit than the spectral type 2 category, so I used the spectral type 3 template for this system.

Spectral Type	# West Spectra in template	# of targets
0	17	0
1	15	0
2	23	0
3	38*	11**
4	55	22
5	32	11
6+	9	12

Notes: * There were originally 41 stars in the spectral type 3 category for the West Spectra, but three were removed due to NAN values in their spectra interfering with the fitting. **SDSS J102857.78+093129.8 had M dwarf spectral type 2.5, but the M3 spectral type template was used for this star.

the spectra used in the template at each wavelength) is used as the uncertainty of the M dwarf continuum, as this value dominated over the difference in flux over the wavelength range.

With this, we have everything needed to recover the expected WD Ca II K EWs. Using 10,000 resamples for each target, I allowed the total continuum, M dwarf continuum, total Ca II K EW, and M dwarf Ca II K EW to vary within Gaussian distributions centered on their mean value, and with standard deviation equal to their uncertainty. I set the WD continuum to be equal to the difference between the M dwarf continuum and the total continuum. The WD Ca II K EW was set to be the median of these 10,000 resamples, and the WD Ca II K EW uncertainty was set

to be the median average deviation of these 10,000 resamples.

2.2.3 Obtaining White Dwarf Calcium Abundance Using Polluted White Dwarf Models

I am able to recover WD calcium abundances for the two systems with clear Ca II K absorption features. SDSS J015225.38-005808.5 and SDSS J184412.58+412029.4 were fitted with polluted WD models, where Simon Blouin (private communication) calculated model atmospheres at the specific T_{eff} and log g values for each of the two WDs. Synthetic spectra with varying Ca/H were calculated for each of the two WDs to match the shape of the Ca II H&K lines. Note that while in general polluted WD models should be calculated using the same atmospheric composition for the model structure calculation and synthetic spectrum, this is not necessary for low to moderate Ca abundances in WDs with hydrogen-dominated atmospheres due to minimal calcium opacity and the fact that calcium provides few free electrons compared to the hydrogen background. For each system, the synthetic spectra were overplotted on the normalized observed spectrum to identify the best-fitting Ca/H value. The uncertainty was determined qualitatively by-eye to determine the range of Ca/H values that give a good fit to the observed spectrum (Simon Blouin, private communication). These WD calcium abundances are applied to equation 2.2.5 to recover the M dwarf wind mass loss rates which are presented in section 3.0.1.

2.2.4 Obtaining M Dwarf Wind Mass-Loss Rates From White Dwarf Calcium Abundances

M dwarf wind mass-loss rates systems with known WD calcium abundances are recovered via the following methodology:

Applying equation 2.2.5 to the system, the WD calcium abundances are used with the other relevant parameters to calculate the M dwarf wind mass-loss rates. The calcium abundance, WD mass, separation, relative velocity, e-folding timescale for calcium, and WD convective zone mass fraction were resampled 10,000 times using the first 10,000 entries from the resampled values previously generated for determining the Roche overflow and calcium detectability confidence. This was done to ensure internal consistency when handling the uncertainties associated with the e-folding timescale and the WD convective zone mass fraction. Since these two parameters are found by interpolating the Bauer & Bildsten (2019) tables for the WD mass and effective temperature combination, the resampled e-folding timescales and convective zone mass fractions are dependent on the resampled WD mass and WD effective temperature. I wanted the resampled e-folding timescales and convective zone mass fractions to align with the resampled WD masses that they were derived from when considering the overall uncertainty of the wind mass-loss rates, which is why I opted to reuse the resampled values generated for the Roche overflow and calcium detectability checks. The median of the wind mass-loss rates found for the resampled parameters was used for the reported M dwarf wind mass-loss rate, and the median average deviation was used for the uncertainty.

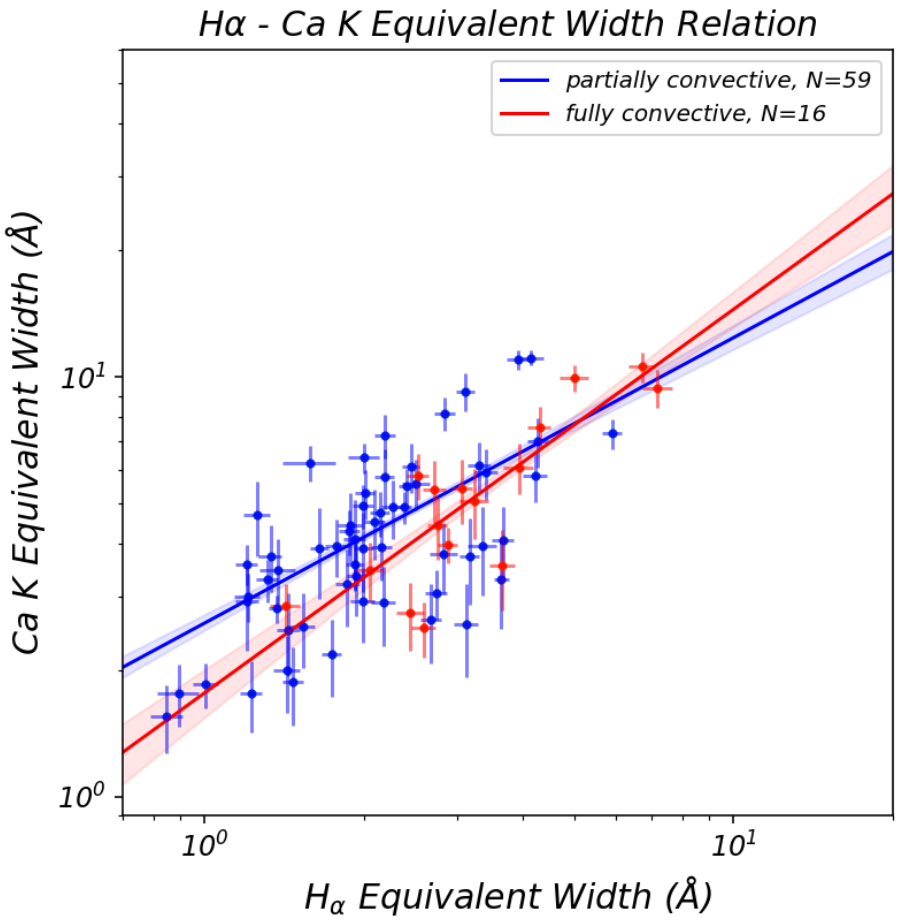

Figure 2.7: M dwarf calcium emission EW as a function of M dwarf Hα emission EW with best fit line and fit error. The Ca K EW and Hα EW of the systems used to define the correlation are shown as dots with their individual uncertainties. The partially convective M dwarfs are shown in blue and the fully convective M dwarfs are shown in red.

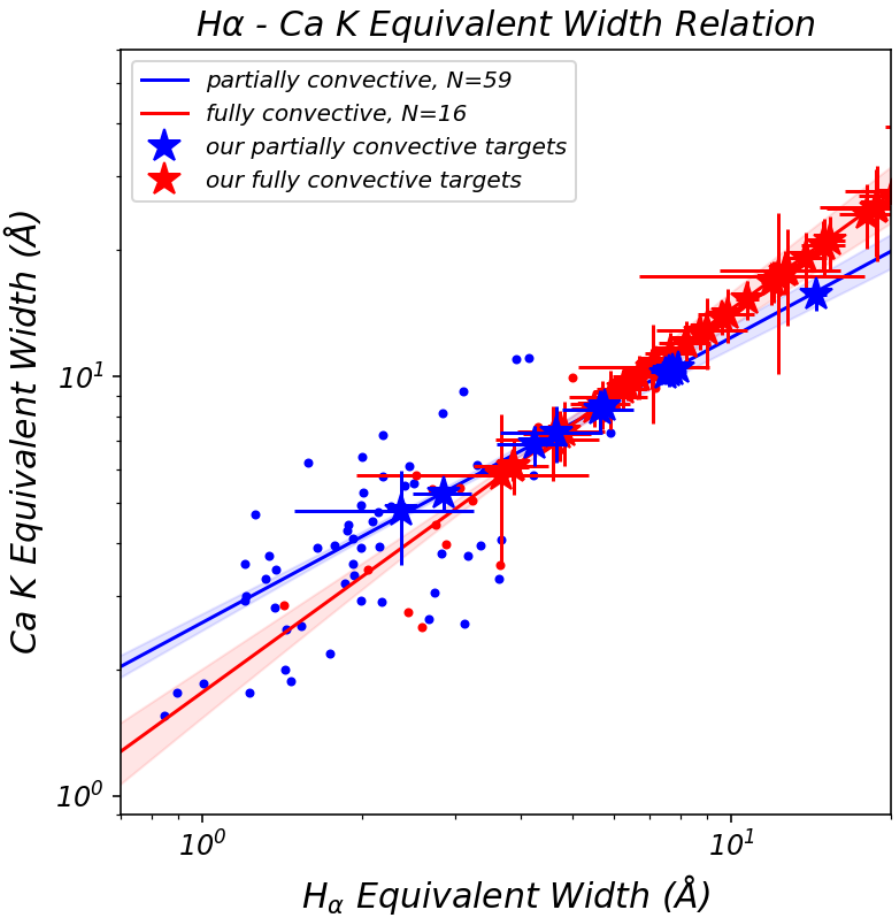

Figure 2.8: The magnetically active M dwarfs from West et al. (2011) are shown as dots, with blue for partially convective and red for fully convective. Our Hα - Ca II K EW correlations for partially and fully convective M dwarfs and the correlation uncertainties are shown as the blue and red lines, respectively. My M dwarf isolated Hα EWs are fitted to the correlation corresponding to their spectral type, shown as stars along with their Hα and Ca II K EW uncertainties. All my systems are above the 3 Å calcium EW threshold suggested by Rauscher & Marcy (2006). Note that some of the target M dwarf Hα EWs are too large to be shown on this plot.

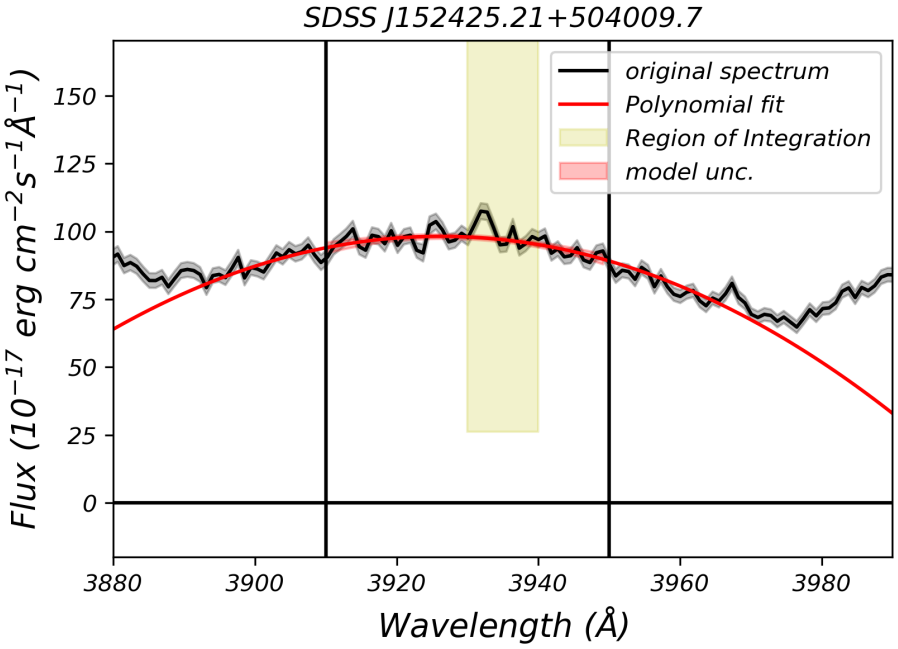

Figure 2.9: My polynomial fit to the local continuum in the Ca II K region. The WD+MD spectrum and uncertainty are shown in black. The polynomial fit and uncertainty are shown in red. The black vertical bars show the region where the model is fit to the WD+MD spectrum. Points within the yellow shaded box are not considered for the model fit, as this is where the calcium emission and absorption features occur. The yellow shaded box also highlights the region of integration for determining the total WD+MD Ca II K EW.

Chapter 3

Results

I will now present the results of the two core methodologies discussed in sections 2.2.2 and 2.2.3: obtaining WD calcium abundances from spectral synthesis fitting and M dwarf wind mass-loss rates from the sample with visible calcium absorption lines, and obtaining WD Ca II K EWs in the platinum, gold, silver 1, and silver 2 samples.

3.0.1 Visible Ca Sample

The WD calcium abundances for the two systems with clear WD calcium absorption lines were obtained using the methodology described in section 2.2.3 by Simon Blouin (private communication). For all other systems, WD calcium absorption lines were not present, or not deep enough to be fit by the polluted WD models confidently. I calculated the wind mass-loss rate values by applying equation 2.2.5 to these systems, as described in section 2.2.4. The calcium abundances and M dwarf wind mass-loss rates are presented in table 3.1.

SDSS J015225.38-005808.5

SDSS J015225.38-005808.5 has a WD log g of 8.19 ± 0.09 (g in units of cm/s^2) and a WD effective temperature of 8773 ± 25 K reported in the SDSS WDMS binary catalogue. Using the reported log g and T_{eff} values, the calcium absorption lines for this system were best fit by an abundance of log N(Ca)/N(H)= -10.2 ± 0.3 as shown in figure 3.1. The orbital period of this system in the SDSS WDMS binary catalogue is $p_{orb} = 2.15195 \pm 0.00001$ hours. Combined with the WD mass of 0.72 ± 0.059 M$_\odot$ and M dwarf mass of 0.102 ± 0.015 M$_\odot$ this results in a pair separation of 0.00367 ± 0.00009 AU using equation 2.2.2. A relative velocity of 695 ± 39 km/s is found using equation 2.2.8, where the separation and orbital period previously mentioned are used to find the orbital velocity in equation 2.2.6, and the previously mentioned M dwarf mass is used along with the M dwarf radius 0.137 ± 0.015 R$_\odot$ in equation 2.2.7 to calculate the M dwarf escape velocity. The calcium e-folding timescale and white dwarf convective zone mass fraction were found using the WD mass and effective temperature values previously discussed, providing the final values needed to calculated the M dwarf wind rate using equation 2.2.5. The wind mass-loss rate for this system was calculated to be $\dot{M}_{MD} = (6.2 \pm 2.8) \times 10^{-17}\ M_\odot/yr$.

SDSS J184412.58+412029.4

SDSS J184412.58+412029.4 has a WD log g of 7.49 ± 0.055 (g in units of cm/s^2) and a WD effective temperature of 7554 ± 6 K reported in the SDSS WDMS binary catalogue (Rebassa-Mansergas et al., 2012). Using the reported log g and T_{eff} values, the calcium absorption lines for this system were best fit by an abundance of log N(Ca)/N(H)= -10.2 ± 0.2 as shown in figure 3.2. The orbital period of this system

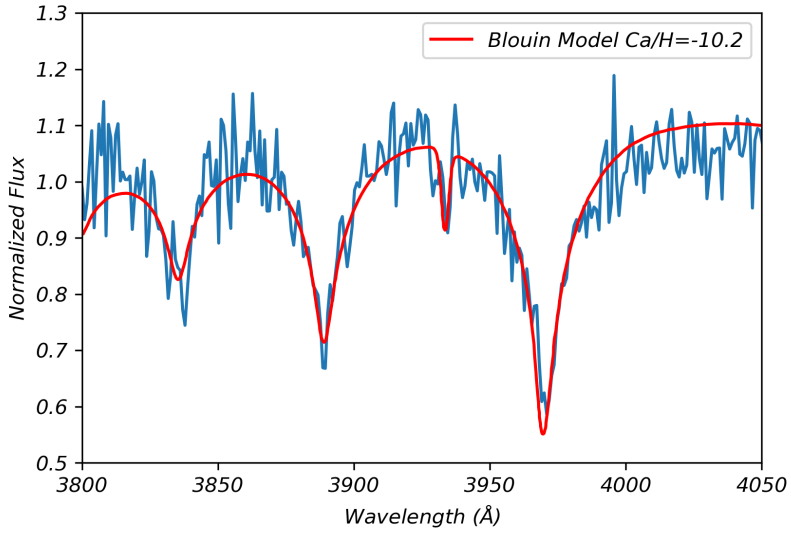

Figure 3.1: The normalized spectrum of SDSS J015225.38-005808.5 with the best fitting Blouin polluted WD model shown in red (Simon Blouin, private communication).

in the SDSS WDMS binary catalogue is $p_{orb} = 5.417 \pm 0.001$ hours. Combined with the WD mass of 0.34 ± 0.021 $M_\odot$ and M dwarf mass of 0.102 ± 0.015 $M_\odot$ this results in a pair separation of 0.0055 ± 0.0001 AU using equation 2.2.2. A relative velocity of 596 ± 44 km/s is found using equation 2.2.8, where the separation and orbital period previously mentioned are used to find the orbital velocity in equation 2.2.6, and the previously mentioned M dwarf mass is used along with the M dwarf radius 0.137 ± 0.015 $R_\odot$ in equation 2.2.7 to find the M dwarf escape velocity. The calcium e-folding timescale and white dwarf convective zone mass fraction were found using the WD mass and effective temperature values previously discussed, providing the final values needed to calculated the M dwarf wind rate using 2.2.5. The wind mass-loss rate for this system was calculated to be $\dot{M}_{MD} = (18.5 \pm 6.6) \times 10^{-17}\ M_\odot/yr$.

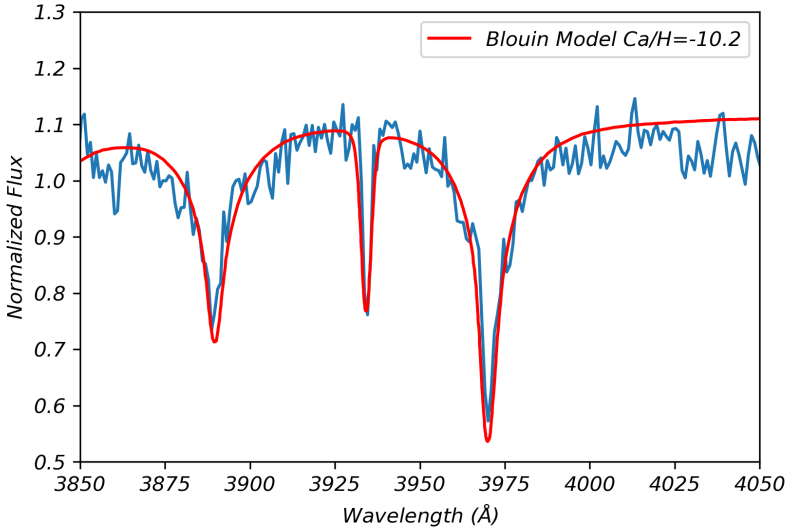

Figure 3.2: The normalized spectrum of SDSS J184412.58+412029.4 with the best fitting Blouin polluted WD model shown in red (Simon Blouin, private communication).

Table 3.1: This table presents the calcium abundances and calculated M dwarf wind mass-loss rates for the two targets with calcium absorption features strong enough to be fit by the Blouin models.

System	Ca/H	$\dot{M}_{MD}$ $(M_{\odot}/yr)$
SDSS J015225.38-005808.5	-10.2 ± 0.3	$(6.21 \pm 2.84) \times 10^{-17}$
SDSS J184412.58+412029.4	-10.2 ± 0.2	$(18.53 \pm 6.62) \times 10^{-17}$

3.0.2 Platinum, Gold, Silver 1, Silver 2

I calculated the WD calcium equivalent widths for a total of 56 systems using the methodology described in section 2.2.2. Of these, 28 are from the platinum sample, 18 from the gold sample, and 10 from the silver 1 sample. Recall that while the conditions for the gold sample encompass the platinum sample, and the conditions for the silver 1 sample encompass the gold sample, we refer to targets by the most rigorously constrained sample that they are in. By this convention, these three samples have no overlapping targets with one another. The silver 2 sample contains 8 systems that are each contained in one of the gold or silver 1 samples. Though the WD calcium EWs are calculated for each of the 56 systems, not all of them result in absorption. 31 of the 56 systems have WD calcium EWs that are above 0 (absorption), with 19 of these yielding absorption at the 1σ level. Using the total Ca II K EW of SDSS J015225.38-005808.5 (0.38 Å) as a detectability threshold for my WD Ca II K EWs, 13 of my systems have WD absorption that should be detectable in the absence of their M dwarf companion. Of these, 12 systems also have WD Ca absorption EWs at the 1σ level, two of which are the targets from the Visible Ca sample. The WD Ca II K EWs and uncertainties are summarized in table 3.2, and in figure 3.3 for visualization purposes.

Table 3.2: Each of my targets presented with the expected WD Ca II K EW and uncertainty, which samples it is a member of, and whether absorption is expected within the 1σ uncertainties.

System	WD EW (Å)	Samples	absorption
SDSS J100609.18+004417.0	-0.51 ± 0.19	gold, silver 2	no
SDSS J152359.22+460448.9	0.10 ± 0.13	gold, silver 2	no
SDSS J015225.38-005808.5	0.71 ± 0.13	gold, silver 2, visible Ca	yes
SDSS J115156.94-000725.4	0.08 ± 0.17	platinum	no
SDSS J151921.72+353625.8	-0.16 ± 0.10	platinum	no
SDSS J154846.00+405728.8	0.19 ± 0.29	platinum	no
SDSS J160821.47+085149.9	0.17 ± 0.29	gold, silver 2	no
SDSS J161145.88+010327.8	-0.47 ± 0.25	gold	no
SDSS J211205.31+101427.9	-0.27 ± 0.24	platinum	no
SDSS J212320.74+002455.5	-0.43 ± 0.37	platinum	no
SDSS J162552.91+640024.9	-0.30 ± 0.21	gold, silver 2	no
SDSS J184412.58+412029.4	0.99 ± 0.08	gold, silver 2, visible Ca	yes
SDSS J032038.72-063822.9	0.16 ± 0.45	gold	no
SDSS J094634.49+203003.4	0.26 ± 0.16	gold	yes
SDSS J104738.24+052320.3	-0.76 ± 0.38	gold	no
SDSS J105756.93+130703.5	-0.76 ± 0.31	platinum	no
SDSS J141451.73-013242.7	0.42 ± 0.44	gold	no
SDSS J143547.87+373338.5	0.56 ± 0.11	platinum	yes
SDSS J152933.25+002031.2	-0.00 ± 0.13	platinum	no
SDSS J164615.60+422349.2	-0.35 ± 0.14	platinum	no

Continued on the next page

Continued from previous page

System	WD EW (Å)	Samples	absorption
SDSS J170509.65+210904.4	0.13 ± 0.08	silver 1	yes
SDSS J221616.59+010205.6	-0.09 ± 0.08	platinum	no
SDSS J224038.37-093541.4	-0.05 ± 0.13	platinum	no
SDSS J030544.41-074941.2	0.25 ± 0.16	platinum	yes
SDSS J083354.84+070240.1	0.08 ± 0.27	platinum	no
SDSS J092452.39+002449.0	-0.62 ± 0.14	gold	no
SDSS J094913.37+032254.5	0.58 ± 0.29	platinum	yes
SDSS J114312.57+000926.5	0.31 ± 0.15	platinum	yes
SDSS J121258.25-012310.2	-0.07 ± 0.07	platinum	no
SDSS J123139.80-031000.3	-1.01 ± 0.57	silver 1	no
SDSS J131334.74+023750.7	1.16 ± 0.17	platinum	yes
SDSS J143443.24+533521.2	-0.09 ± 0.05	silver 1	no
SDSS J143746.69+573706.0	0.29 ± 0.23	gold	yes
SDSS J150657.58-012021.7	0.33 ± 0.37	platinum	no
SDSS J152425.21+504009.7	-0.12 ± 0.07	silver 1	no
SDSS J171810.15+610114.0	0.43 ± 0.24	platinum	yes
SDSS J173101.49+623315.9	0.79 ± 0.29	platinum	yes
SDSS J212051.92-005827.3	0.08 ± 0.08	platinum	no
SDSS J213218.11+003158.8	0.29 ± 0.14	platinum	yes
SDSS J233928.35-002040.0	-0.32 ± 0.32	gold	no
SDSS J030138.24+050218.9	-0.09 ± 0.17	gold	no

Continued on the next page

Continued from previous page

System	WD EW (Å)	Samples	absorption
SDSS J130012.49+190857.4	0.92 ± 0.31	gold, silver 2	yes
SDSS J134841.61+183410.5	-0.25 ± 0.09	platinum	no
SDSS J155808.49+264225.7	-0.70 ± 0.41	platinum	no
SDSS J162354.45+630640.4	0.82 ± 0.29	silver 1, silver 2	yes
SDSS J023804.39-000545.7	0.46 ± 0.23	silver 1	yes
SDSS J024642.55+004137.2	0.22 ± 0.62	platinum	no
SDSS J080736.96+072412.0	1.00 ± 0.29	platinum	yes
SDSS J121130.94-024954.4	-0.86 ± 0.50	silver 1	no
SDSS J222108.45+002927.7	0.21 ± 0.28	gold	no
SDSS J231825.23-093539.1	0.23 ± 0.15	silver 1	yes
SDSS J030716.44+384822.8	-4.63 ± 1.06	silver 1	no
SDSS J110517.60+385125.7	0.66 ± 0.14	gold	yes
SDSS J142951.19+575949.0	0.38 ± 0.60	platinum	no
SDSS J231105.66+220208.6	-0.51 ± 0.20	silver 1	no
SDSS J102857.78+093129.8	-1.34 ± 0.23	platinum	no

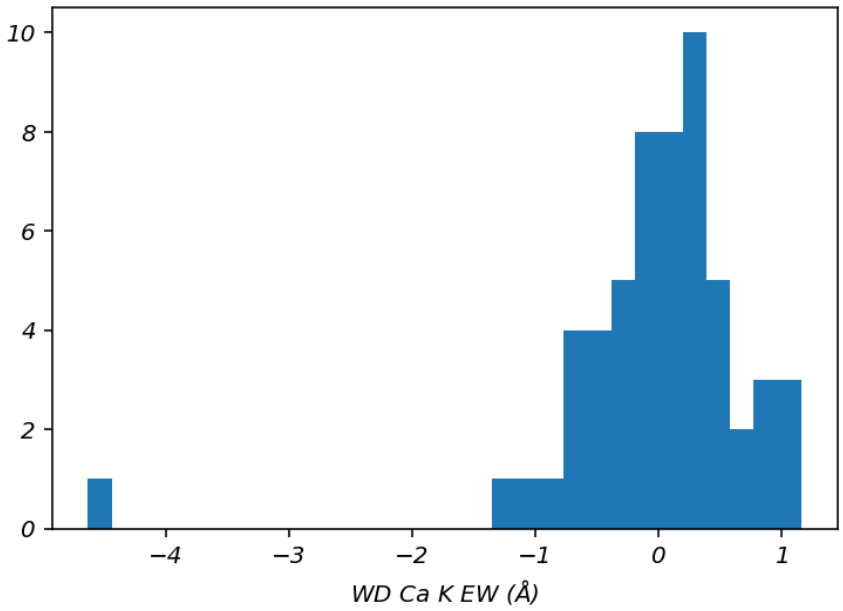

Figure 3.3: A histogram showing the WD EW values from table 3.2. Recall that negative values are emission and positive values are absorption.

Chapter 4

Discussion

4.1 Interpretation of Results

4.1.1 Wind Rates

The two M dwarf wind mass-loss rates I calculated constitute some of the lowest M dwarf wind rates published to date, as seen in figure 4.1. Compared to these published M dwarf wind rates, my result for the wind mass-loss rate of SDSS J015225.38-005808.5 is consistent with the lowest two literature M dwarf wind mass-loss rates and my result for the wind mass-loss rate of SDSS J184412.58+412029.4 is in the lowest $\sim 15\%$ of literature M dwarf wind mass-loss rates, as shown in figure 4.2.

The methodology used to determine M dwarf wind mass-loss rates for the three close WD+MD binaries in D06 and the methodology used to determine M dwarf wind mass-loss rates using the BHL accretion model in W23 are most similar to the methodology used in this work. These PCEB systems seem especially promising in their ability to probe lower M dwarf wind mass-loss regimes. Figure 4.1 shows that most of

the lowest M dwarf wind mass-loss rates detected to date have been found using the PCEB method. This is especially true when we consider that the wind mass-loss rates found from the slingshot prominence method are likely to be underestimated, as discussed in section 1.1.1. Figure 4.3 shows the literature PCEB wind rates compared to the two M dwarf wind rates calculated in this work as a function of orbital period. There are no clear trends between the calculated wind mass-loss rates and the orbital periods. I expect that systems with longer orbital periods may be more biased towards higher wind rates, since systems with wider separations accrete a lower fraction of the M dwarf wind material onto the WD. Since the wind material density decreases while moving away from the M dwarf, systems with wider separations (longer orbital periods) would require a larger M dwarf wind mass-loss rate to produce a detectable absorption signature in the WD than systems with shorter orbital periods.

While it is apparent that M dwarf wind mass loss rates span a huge range, recent works have been consistently pushing the lower limits of what wind rates can be recovered. These lower wind rates make the possibility of HZ planets retaining their atmospheres more promising. As methodologies are developed which can probe lower and lower wind rates, the true distribution of M dwarf wind rates will hopefully be revealed.

One potential issue with my results is that the recovered wind rates do not account for any contribution from the M dwarf in the Ca II K line. As discussed in section 2.2.2, magnetically active M dwarfs can produce emission in the Ca II H&K lines. If there is an M dwarf emission contribution in SDSS J015225.38-005808.5 and SDSS J184412.58+412029.4, then their calcium abundances and wind mass-loss rates are likely underestimated. Since both these targets are also contained in the gold sample

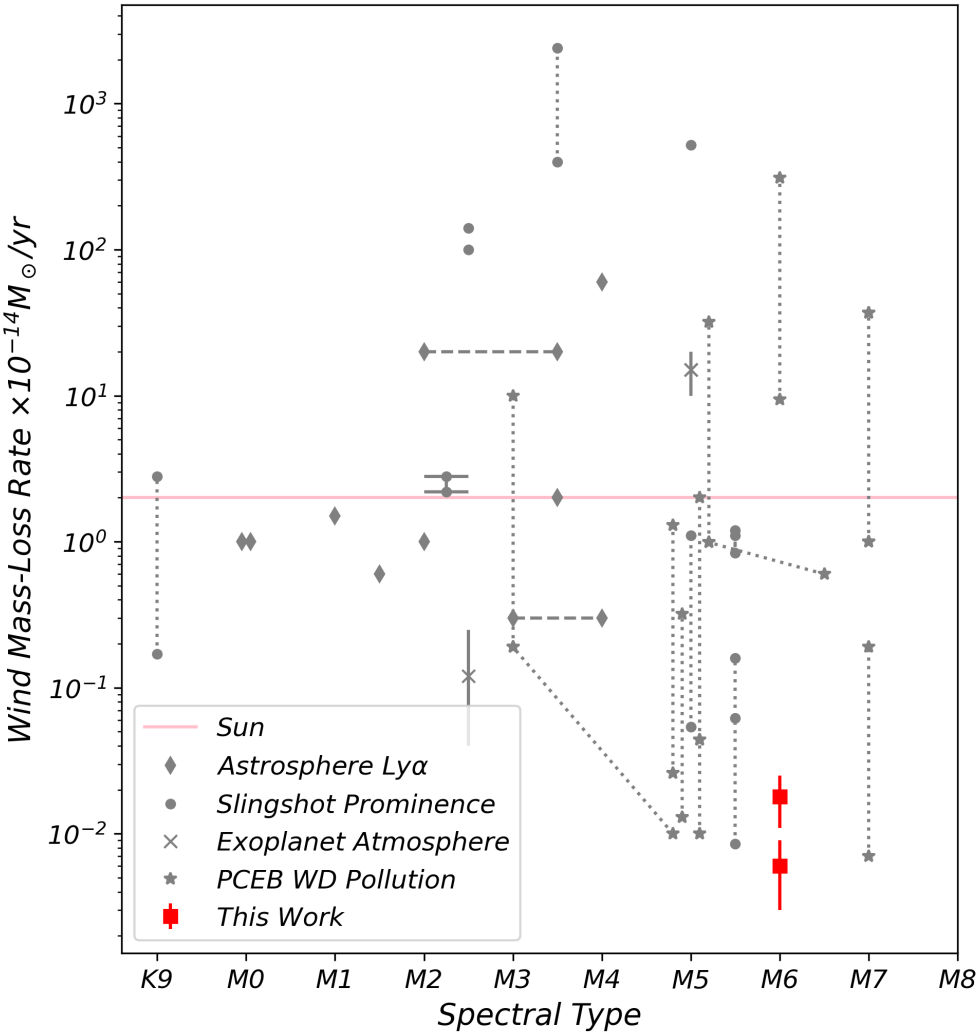

Figure 4.1: M dwarf wind rates from the literature (see figure 1.1) with results from this work shown in red. The Sun's rate is shown as a pink horizontal line for reference.

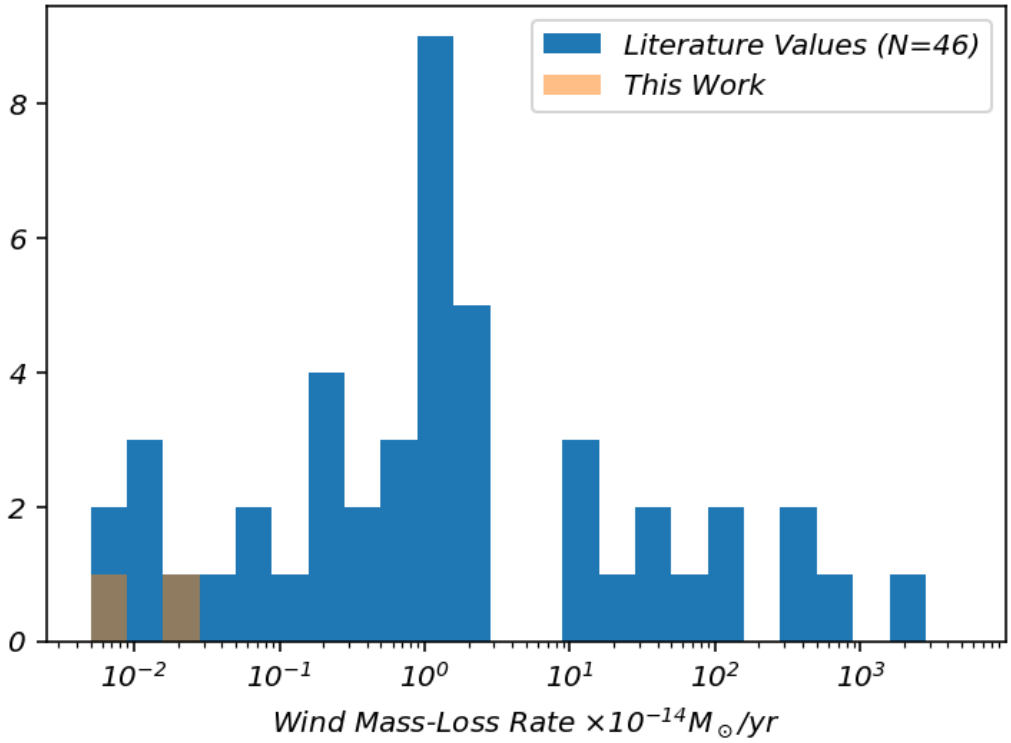

Figure 4.2: A histogram showing our two M dwarf wind mass-loss rates compared to the distribution of literature M dwarf wind mass-loss rates.

and silver 2 sample, it should be possible for a future work to quantify by how much these wind rates may be underestimated. See section 4.2 for further discussion.

Another potential issue with my results is that the M dwarfs I have calculated wind rates for are not field stars. The common-envelope phase that these systems experienced prior to the formation of the WD may have altered the magnetic properties and wind rate of the M dwarf. However, these wind rates may be compared to wind rates of M dwarfs with similar activity levels, such as young M dwarfs that aren't in a close binary system.

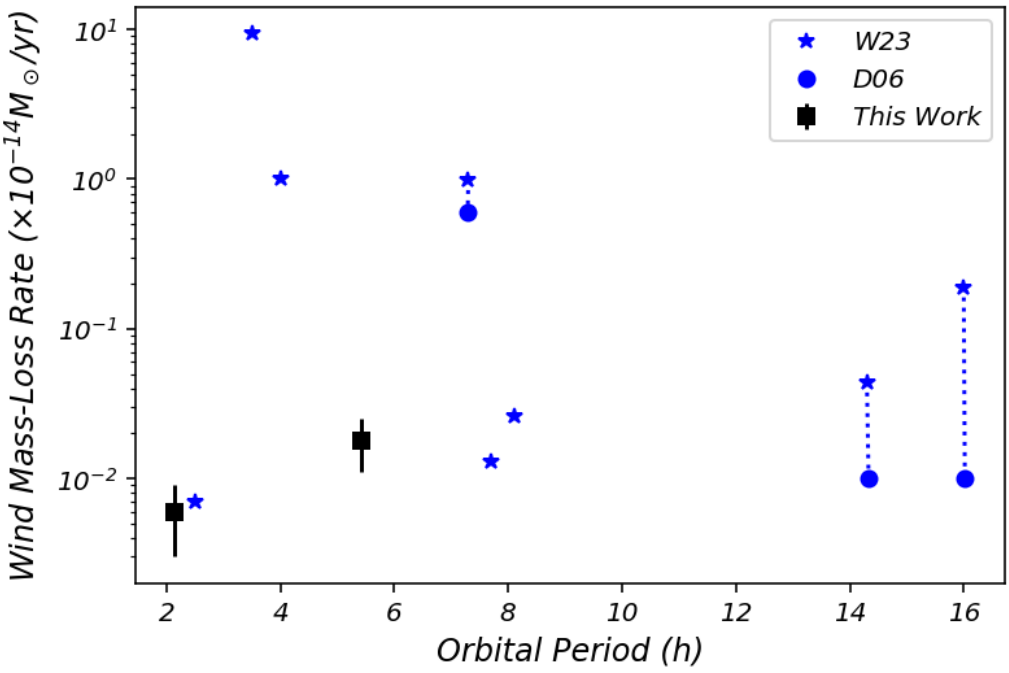

Figure 4.3: Our M dwarf wind mass-loss rates (black squares) compared to the W23 M dwarf wind mass-loss rates found using the BHL accretion model (blue stars) and the D06 M dwarf wind mass-loss rates found in close WD+MD binaries (blue circles) as a function of orbital period. Systems observed in both D06 and W23 are connected by dotted lines. Orbital period was used instead of binary separation because the separation values were not listed in W23.

4.1.2 White Dwarf Calcium Equivalent Widths

As discussed in 3.0.2 there are 19 systems that show Ca II K absorption at the 1σ level from my initial selection of 56 promising systems. Of these, 11 also have Ca II K absorption EWs greater than the EW of SDSS J015225.38-005808.5 (the system with the smaller calcium absorption feature that was able to be fit by the Blouin polluted WD models, EW= 0.38 Å), suggesting that if these WD were able to be observed independently from their M dwarf companions their calcium absorption would be detectable with SDSS. In figure 4.4 I show the distribution of my sample compared

to isolated and binary member WDs from Zuckerman et al. (2003). While I expect that only the 11 targets with WD Ca II K EW> 0.38 Å have large enough absorption features to be detectable with SDSS (in the absence of the M dwarf emission), the sensitivity of the Zuckerman et al. (2003) results to EWs of tens of mÅ suggests that a larger telescope might be able to detect all 19 WD absorption features in the absence of the M dwarf emission.

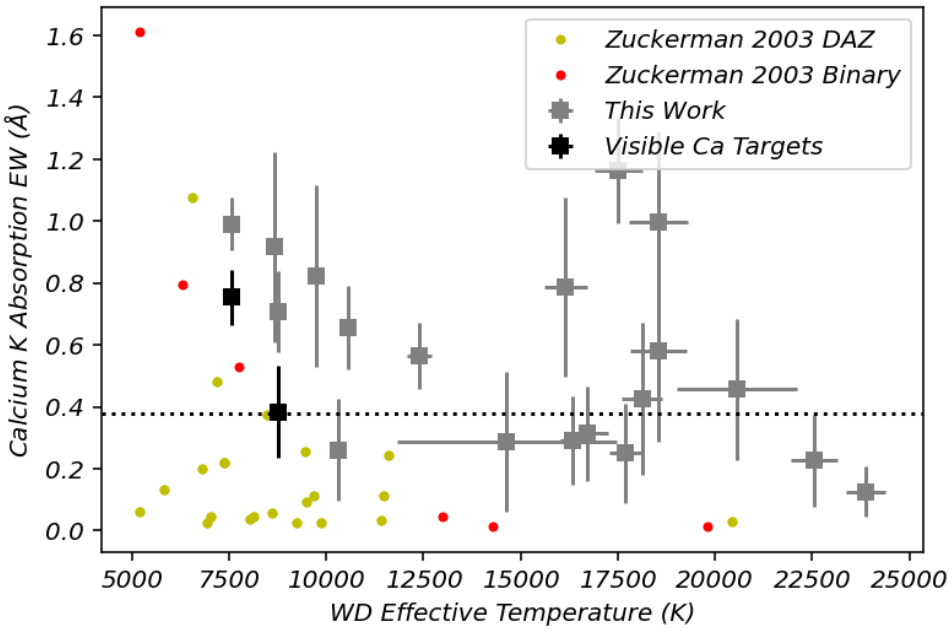

Figure 4.4: WD Ca II K absorption EWs as a function of WD effective temperature for my sample (grey squares) compared to the values reported in table 1 of Zuckerman et al. (2003) for isolated DAZ (yellow dots) and the table 2 values for WDs in binary systems (red dots). My visible Ca targets are shown in black squares for reference. The horizontal dashed line shows my estimated SDSS detectability threshold.

While it is not be possible to resolve these WDs independently from their close M dwarf companions, it may still be possible to directly detect the WD calcium contributions. As is seen with SDSS J164615.60+422349.2 in figure 1.2, M dwarf emission

features can change with time. If it is possible to observe these systems during a time with minimal M dwarf emission, especially with a high resolution spectrograph, it may be possible to directly detect WD Ca II K absorption for these systems.

4.2 Future Work

Having a good handle on the expected WD Ca II K absorption EWs, I believe it will be possible for a future work to recover M dwarf wind mass-loss rates for the 19 systems showing Ca II K absorption at the 1σ level. By using polluted WD models, such as those provided by Simon Blouin (Blouin et al., 2018a,b, 2019a,b), a series of spectra can be calculated for each system based on their known effective temperature and surface gravity and varying the Ca/H values. Instead of matching the best-fitting Ca/H value to the absorption feature by-eye (as done in section 2.2.3) the calcium absorption EW of each model can be calculated using the methodology described in section 2.2.2. The Ca abundances can be recovered by matching the model EWs to the observed WD Ca II K EW. From there, following the methodology described in section 2.2.4, the wind rates for these systems could be calculated.

A further extension of calculating these wind rates would be to compare the wind mass-loss rates for SDSS J015225.38-005808.5 and SDSS J184412.58+412029.4 found using the WD Ca EWs versus the wind mass-loss rates reported in this work. Since none of the previously published M dwarf wind mass-loss rates found using pollution of a close WD companion have considered potential M dwarf Ca emission lines, it is possible that all these values are underestimated. Recall that Rebassa-Mansergas et al. (2013) suggest that all M dwarfs in PCEB systems are magnetically active (section 1.3.1). From my own look at PCEB systems with an M dwarf companion, a

clear majority of the systems show emission at least in the Hα line, suggesting that many are magnetically active. For this reason, it is important to consider than many of the previously published M dwarf wind rates using this methodology may be lower than the true value.

Another piece of this methodology that could be improved is the EW relation between Hα and Ca II K in magnetically active M dwarfs. As is clear from 3.2, over half of the WD Ca II K EWs are negative, indicating emission. This suggests that this work may be underestimating the amount of M dwarf calcium emission. My choice in uncertainty constraints was motivated by wanting to derive the EW correlation on systems with low absolute and relative uncertainties. However, since my PCEB targets are biased towards systems with large Hα EW, it may have been better to derive the EW correlation on a sample of M dwarfs biased towards large Hα EW as well.

Another component to consider in a future work would be the M dwarf wind velocity assumption. In this work, I assumed that the M dwarf wind had a velocity equal to the escape velocity of the M dwarf. The wind velocities used in this work spanned $\sim 550-730$ km/s. However, works such as Bourrier et al. (2016) calculate much lower wind velocities ($\sim 70-90$ km/s) for the M dwarf GJ 436, while Harbach et al. (2021) calculate higher wind velocities ($\sim 700-1100$ km/s) for the M dwarf TRAPPIST 1. Hydrodynamic modeling of the stellar wind and stellar magnetic B-field for a few test cases based on different stellar masses and magnetic field strengths could provide better velocity estimates than the escape velocity, which ignores all magnetic effects. For future observations, there are two components that I believe would provide the greatest insight. Higher resolution spectra, such as from the Keck telescope HIRES

echelle spectrograph, have sufficient resolution to individually resolve the M dwarf emission and WD absorption components in the Ca II K&H lines for the WD+M star system WD 0419-487, as shown in figure 3 of Zuckerman et al. (2003). Repeat observations of the same system provide the opportunity for better orbital characterization and allow for the monitoring of M dwarf emission line changes over time for individual systems. Observing a previously active system at a moment of M dwarf quiescence could allow for WD absorption features that were previously hidden by the M dwarf emission features to be observed directly, allowing for a direct fit using polluted WD models. Since the diffusion timescale of calcium is highly sensitive to the WD effective temperature and surface gravity, some systems have short enough diffusion timescales (< 1 day) that the different wind rates before and during quiescence could be measured independently, while others have much longer diffusion timescales (> 100 years) and would result in an average wind rate, since M dwarf emission line changes tend to be < 200 days for short-term variability (Mignon et al., 2023).

4.3 Conclusions

In addition to contributing two of the lowest M dwarf wind mass-loss rates published to date, this project has improved the methodologies introduced in D06, allowing a wider variety of systems to be considered. While the wind rates for my PCEB targets without visible Ca absorption have not been calculated in this work, I have laid the groundwork for how these wind rates could be recovered. Being able to calculate M dwarf wind rates in PCEB systems with M dwarf emission lines will greatly expand

the pool of targets, especially because so many M dwarfs in PCEB systems are magnetically active. This will greatly expand the set of existing measurement of M dwarf wind mass-loss rates and improve our understanding of the true distribution of M dwarf wind rates.

Our two recovered wind rates are especially interesting when considering star-planet interactions. Works such as Chin et al. (2024) opt not to calculate planet atmospheric escape around M dwarfs due to the diversity of wind conditions, instead using stellar wind conditions of the young Sun. Based on my results, the wind mass-loss rates of M dwarfs can be several orders of magnitude lower than that of the young Sun, indicating that at least for some M dwarf stars, wind driven exoplanet atmosphere loss rates should be much lower than those predicted by Chin et al. (2024). Zendejas et al. (2010) calculate atmospheric mass loss for planets around M dwarf stars with a time-dependent stellar wind and a time-independent stellar wind. They assume stellar wind mass-loss rates ~ 6 orders of magnitude higher than my calculated values, although it should be noted that they are interested in the mass-loss rates of young M dwarfs, while my wind rates are for much older stars. However, the stars I calculate wind rates for are late type M dwarfs, which are known to remain active for 4-8 Gyr (West et al., 2008). Indeed, both my wind rates come from magnetically active M dwarfs, indicated by their Hα emission lines. This suggests that wind rates in magnetically active M dwarfs can be much lower than typically assumed, challenging the conclusion that HZ planets around late type M dwarfs are unlikely to retain their atmospheres for 1 Gyr or more. As lower M dwarf wind mass-loss rates continue to be discovered, the possibility of M dwarf HZ planets retaining their atmospheres seems more promising.

We still have much to learn about M dwarf stellar wind mass-loss rates before we can attain an unbiased population level understanding. WD+MD PCEB systems are particularly promising for exploring the regime of magnetically active M dwarfs, and may mimic the wind conditions of young M dwarfs, a crucial population for understanding how M dwarf winds sculpt exoplanet atmospheres.

Appendix A

Table A.1: All literature values of M dwarf wind mass-loss rates with the same units, and with the M dwarf spectral type, or types for binary systems. References: (1) Wood et al. (2005) (2) Vannier et al. (2025) (3) Wood et al. (2021) (4) Jardine & Collier Cameron (2019) (5) Waugh et al. (2021) (6) Bourrier et al. (2016) (7) Vidotto & Bourrier (2017) (8) Alvarado-Gómez et al. (2022) (9) Debes (2006) (10) Walters et al. (2023) (11) This Work

Star	Spectral Type	$\dot{M}_{MD}$ (10^{-14} $M_\odot$ yr^{-1})	Ref
EV Lac	M3.5	2	1
GJ 173	M1	1.5	2 & 3
GJ 338AB	M0 + M0	1	3
YZ CMi	M4	60	3
GJ 205	M1.5	0.6	3
GJ 860AB	M3 + M4	0.3	3
GJ 15AB	M2 + M3.5	20	3
GJ 887	M2	1	3
HK Aqr	M2.5	100	4
V374 Peg	M3.5	400	4

Continued on the next page

Continued from previous page

Star	Spectral Type	$\dot{M}$ (10^{-14} $M_\odot$ yr^{-1})	Ref
V374 Peg	M3.5	2400	5
EQ Peg B	M5	520	5
GJ1156	M5.5	1.1, 0.84, 1.2	5
AD Leo	M2 or M2.5	2.2, 2.8	5
EQ Peg A	M2.5	140	5
GJ1111	M5	0.054, 1.1	5
GJ1245b	M5.5	0.0085, 0.16, 0.062	5
GJ9520	M0.5	3.6	5
GJ494	K9	0.17, 2.8	5
GJ 436	M2.5	0.045-0.25	6 & 7
AU Mic	M5	$\sim$ 10-20	8
WD 0419-487	M6.5	0.6	9
LHS 1660 (WD 0419-487)	M5	0.99 - 32	10
WD 1026+002	M5	0.01	9
PG 1026+002 (WD 1026+002)	M5	0.044 - 2.0	10
WD 1213+528	M5	0.01	9
Case 1 (WD 1213+528)	M3	0.19 - 10	10
Rubin 80 (WD 0354+463)	M7	1.0 - 37	10
LTT 560	M6	9.4 - 310	10
PG 2257+162	M5	0.013 - 0.32	10

Continued on the next page

Continued from previous page

Star	Spectral Type	$\dot{M}$ (10^{-14} $M_\odot$ yr^{-1})	Ref
BPM 6502	M5	0.026 - 1.3	10
GD 448	M7	0.0070 - 0.19	10
SDSS J015225.38-005808.5	M6	0.006±0.003	11
SDSS J184412.58+412029.4	M6	0.018±0.007	11

Bibliography

Alvarado-Gómez J. D., et al., 2022, ApJ, 928, 147

Ashley R. P., Farihi J., Marsh T. R., Wilson D. J., Gänsicke B. T., 2019, MNRAS, 484, 5362

Asplund M., Grevesse N., Sauval A. J., Scott P., 2009, ARA&A, 47, 481

Baraffe I., Chabrier G., 1996, ApJL, 461, L51

Barnes S., Sofia S., 1996, ApJ, 462, 746

Bauer E. B., Bildsten L., 2019, ApJ, 872, 96

Bédard A., Bergeron P., Brassard P., Fontaine G., 2020, ApJ, 901, 93

Benvenuto O. G., De Vito M. A., 2005, MNRAS, 362, 891

Bergeron P., Wesemael F., Beauchamp A., 1995, PASP, 107, 1047

Bloot S., Vedantham H. K., Kavanagh R. D., Callingham J. R., Pope B. J. S., 2025, A&A, 695, A176

Blouin S., Dufour P., Allard N. F., 2018a, ApJ, 863, 184

Blouin S., Dufour P., Allard N. F., Kilic M., 2018b, ApJ, 867, 161

Blouin S., Dufour P., Allard N. F., Salim S., Rich R. M., Koopmans L. V. E., 2019a, ApJ, 872, 188

Blouin S., Dufour P., Thibeault C., Allard N. F., 2019b, ApJ, 878, 63

Bondi H., 1952, MNRAS, 112, 195

Bondi H., Hoyle F., 1944, MNRAS, 104, 273

Bourrier V., Lecavelier des Etangs A., Ehrenreich D., Tanaka Y. A., Vidotto A. A., 2016, A&A, 591, A121

Bouvier J., Forestini M., Allain S., 1997, A&A, 326, 1023

Butler R. P., Vogt S. S., Marcy G. W., Fischer D. A., Wright J. T., Henry G. W., Laughlin G., Lissauer J. J., 2004, ApJ, 617, 580

Carroll B. W., Ostlie D. A., 2017, An introduction to modern astrophysics, Second Edition

Chabrier G., 2003, PASP, 115, 763

Chabrier G., Baraffe I., 1997, A&A, 327, 1039

Chabrier G., Baraffe I., Plez B., 1996, ApJL, 459, L91

Chandra V., Hwang H.-C., Zakamska N. L., Budavári T., 2020, MNRAS, 497, 2688

Chayer P., Fontaine G., Wesemael F., 1995, ApJS, 99, 189

Chin L., Dong C., Lingam M., 2024, The Astrophysical Journal Letters, 963, L20

Deal M., Deheuvels S., Vauclair G., Vauclair S., Wachlin F. C., 2013, A&A, 557, L12

Debes J. H., 2006, ApJ, 652, 636

Donati J. F., et al., 2023, MNRAS, 525, 2015

Dressing C. D., Charbonneau D., 2015, ApJ, 807, 45

Dufour P., Kilic M., Fontaine G., Bergeron P., Lachapelle F. R., Kleinman S. J., Leggett S. K., 2010, ApJ, 719, 803

Eggleton P. P., 1983, ApJ, 268, 368

Farihi J., 2016, New Astronomy Reviews, 71, 9

Farihi J., Jura M., Zuckerman B., 2009, ApJ, 694, 805

Fontaine G., Michaud G., 1979, ApJ, 231, 826

Foreman-Mackey D., Hogg D. W., Lang D., Goodman J., 2013, PASP, 125, 306

Gillon M., et al., 2007, A&A, 472, L13

Hansen B., 2004, Physics Reports, 399, 1

Harbach L. M., Moschou S. P., Garraffo C., Drake J. J., Alvarado-Gómez J. D., Cohen O., Fraschetti F., 2021, ApJ, 913, 130

Hawley S. L., Gizis J. E., Reid I. N., 1996, AJ, 112, 2799

Henry T. J., Jao W.-C., Subasavage J. P., Beaulieu T. D., Ianna P. A., Costa E., Méndez R. A., 2006, AJ, 132, 2360

Idan I., Lasota J.-P., Hameury J.-M., Shaviv G., 2008, New Astronomy Reviews, 51, 759

Jardine M., Collier Cameron A., 2019, MNRAS, 482, 2853

Jermyn A. S., et al., 2023, ApJS, 265, 15

Johnson T. M., Klein B. L., Koester D., Melis C., Zuckerman B., Jura M., 2022, ApJ, 941, 113

Johnstone C. P., Güdel M., Lüftinger T., Toth G., Brott I., 2015, A&A, 577, A27

Johnstone C. P., Bartel M., Güdel M., 2021, A&A, 649, A96

Kepler S. O., Kleinman S. J., Nitta A., Koester D., Castanheira B. G., Giovannini O., Costa A. F. M., Althaus L., 2007, MNRAS, 375, 1315

Kilic M., von Hippel T., Mullally F., Reach W. T., Kuchner M. J., Winget D. E., Burrows A., 2006, ApJ, 642, 1051

Kislyakova K. G., Güdel M., Koutroumpa D., Carter J. A., Lisse C. M., Boro Saikia S., 2024, Nature Astronomy, 8, 596

Koester D., 2009, A&A, 498, 517

Koester D., 2010, Memorie della Societa Astronomica Italiana, 81, 921

Koester D., Napiwotzki R., Voss B., Homeier D., Reimers D., 2005, A&A, 439, 317

Kopparapu R. k., Wolf E. T., Arney G., Batalha N. E., Haqq-Misra J., Grimm S. L., Heng K., 2017, ApJ, 845, 5

Lamers H. J. G. L. M., Cassinelli J. P., 1999, Introduction to Stellar Winds

Lammer H., et al., 2007, Astrobiology, 7, 185

Laughlin G., Bodenheimer P., Adams F. C., 1997, ApJ, 482, 420

Li J. K., Wu K. W., Wickramasinghe D. T., 1994, MNRAS, 268, 61

Liu Z.-W., Stancliffe R. J., Abate C., Matrozis E., 2017, ApJ, 846, 117

Luger R., Barnes R., 2015, Astrobiology, 15, 119

Lyttleton R. A., 1972, MNRAS, 160, 255

Marvin C. J., Reiners A., Anglada-Escudé G., Jeffers S. V., Boro Saikia S., 2023, A&A, 671, A162

McCook G. P., Sion E. M., 1987, ApJ, 65, 603

Mignon L., et al., 2023, A&A, 675, A168

Modi A., Estrela R., Valio A., 2023, MNRAS, 525, 5168

Morgan D. P., West A. A., Garcés A., Catalán S., Dhital S., Fuchs M., Silvestri N. M., 2012, AJ, 144, 93

Newton E. R., Irwin J., Charbonneau D., Berta-Thompson Z. K., Dittmann J. A., 2016, ApJL, 821, L19

Noor H. T., Farihi J., Hollands M., Toonen S., 2024, MNRAS, 529, 2910

Owen J. E., Wu Y., 2017, ApJ, 847, 29

Paquette C., Pelletier C., Fontaine G., Michaud G., 1986, ApJS, 61, 197

Parker E. N., 1958, ApJ, 128, 664

Parsons S. G., et al., 2012, MNRAS, 420, 3281

Pass E. K., Charbonneau D., Irwin J. M., Winters J. G., 2022, ApJ, 936, 109

Pass E. K., Charbonneau D., Latham D. W., Berlind P., Calkins M. L., Esquerdo G. A., Mink J., 2024, ApJ, 966, 231

Paxton B., Bildsten L., Dotter A., Herwig F., Lesaffre P., Timmes F., 2011, ApJS, 192, 3

Paxton B., et al., 2013, ApJS, 208, 4

Paxton B., et al., 2015, ApJS, 220, 15

Paxton B., et al., 2018, ApJS, 234, 34

Paxton B., et al., 2019, ApJS, 243, 10

Pecaut M. J., Mamajek E. E., 2013, ApJS, 208, 9

Pyrzas S., et al., 2012, MNRAS, 419, 817

Rauscher E., Marcy G. W., 2006, PASP, 118, 617

Rebassa-Mansergas A., Gänsicke B. T., Rodríguez-Gil P., Schreiber M. R., Koester D., 2007, MNRAS, 382, 1377

Rebassa-Mansergas A., Gänsicke B. T., Schreiber M. R., Koester D., Rodríguez-Gil P., 2010, MNRAS, 402, 620

Rebassa-Mansergas A., Nebot Gómez-Morán A., Schreiber M. R., Gänsicke B. T., Schwope A., Gallardo J., Koester D., 2012, MNRAS, 419, 806

Rebassa-Mansergas A., Schreiber M. R., Gänsicke B. T., 2013, MNRAS, 429, 3570

Rebassa-Mansergas A., Ren J. J., Parsons S. G., Gänsicke B. T., Schreiber M. R., García-Berro E., Liu X. W., Koester D., 2016, MNRAS, 458, 3808

Reid N., Hawley S. L., Mateo M., 1995, MNRAS, 272, 828

Ribeiro T., Baptista R., Kafka S., Dufour P., Gianninas A., Fontaine G., 2013, A&A, 556, A34

Sarna M. J., Ergma E., Gerskevits J., 2001, Astronomische Nachrichten, 322, 405

Scargle J. D., 1982, ApJ, 263, 835

Schatzman E., 1945, Annales d'Astrophysique, 8, 143

Schatzman E. L., 1958, White dwarfs

Schreiber M. R., Belloni D., Schwope A. D., 2024, A&A, 682, L7

Sills A., Pinsonneault M. H., Terndrup D. M., 2000, ApJ, 534, 335

Skumanich A., 1972, ApJ, 171, 565

Smolčić V., et al., 2004, ApJ, 615, L141

Stanton L. G., Murillo M. S., 2016, Physical Review E, 93, 043203

Stoughton C., et al., 2002, AJ, 123, 485

Tappert C., Gänsicke B. T., Rebassa-Mansergas A., Schmidtobreick L., Schreiber M. R., 2011a, A&A, 531, A113

Tappert C., Gänsicke B. T., Schmidtobreick L., Ribeiro T., 2011b, A&A, 532, A129

Tarter J. C., et al., 2007, Astrobiology, 7, 30

Theuns T., Boffin H. M. J., Jorissen A., 1996, MNRAS, 280, 1264

Tinker J., Pinsonneault M., Terndrup D., 2002, ApJ, 564, 877

Tremblay P. E., Ludwig H. G., Steffen M., Freytag B., 2013, A&A, 559, A104

Tremblay P. E., Ludwig H. G., Freytag B., Fontaine G., Steffen M., Brassard P., 2015, ApJ, 799, 142

Vanderburg A., et al., 2015, Nature, 526, 546

Vannier H., Redfield S., Wood B. E., Müller H.-R., Linsky J. L., Frisch P. C., 2025, ApJ, 981, 102

Vidotto A. A., Bourrier V., 2017, MNRAS, 470, 4026

Vidotto A. A., Jardine M., Morin J., Donati J. F., Opher M., Gombosi T. I., 2014, MNRAS, 438, 1162

Villaver E., Livio M., 2007, ApJ, 661, 1192

Vincent O., Barstow M. A., Jordan S., Mander C., Bergeron P., Dufour P., 2024, A&A, 682, A5

Wall J. V., Jenkins C. R., 2012, Data modelling and parameter estimation: advanced topics. Cambridge University Press, p. 151–181

Walters N., Farihi J., Dufour P., Pineda J. S., Izzard R. G., 2023, MNRAS, 524, 5096

Waugh R. F. P., Jardine M. M., Morin J., Donati J. F., 2021, MNRAS, 505, 5104

Werner K., Hammer N. J., Nagel T., Rauch T., Dreizler S., 2005, in Koester D., Moehler S., eds, Astronomical Society of the Pacific Conference Series Vol. 334, 14th European Workshop on White Dwarfs. p. 165 (arXiv:astro-ph/0410690), doi:10.48550/arXiv.astro-ph/0410690

West A. A., Hawley S. L., Bochanski J. J., Covey K. R., Reid I. N., Dhital S., Hilton E. J., Masuda M., 2008, AJ, 135, 785

West A. A., et al., 2011, AJ, 141, 97

West A. A., Weisenburger K. L., Irwin J., Berta-Thompson Z. K., Charbonneau D., Dittmann J., Pineda J. S., 2015, ApJ, 812, 3

Winters J. G., et al., 2015, AJ, 149, 5

Wood B. E., Linsky J. L., Müller H.-R., Zank G. P., 2001, ApJ, 547, L49

Wood B. E., Linsky J. L., Müller H.-R., Zank G. P., 2003, ApJ, 591, 1210

Wood B. E., Müller H. R., Zank G. P., Linsky J. L., Redfield S., 2005, ApJ, 628, L143

Wood B. E., et al., 2021, ApJ, 915, 37

Zahnle K. J., Catling D. C., 2017, ApJ, 843, 122

Zendejas J., Segura A., Raga A. C., 2010, Icarus, 210, 539

Zuckerman B., Koester D., Reid I. N., Hünsch M., 2003, ApJ, 596, 477

van Roestel J., et al., 2025, A&A, 696, A242